Journal of
Composites Science

MDPI

Article

Progressive Fatigue Failure Analysis of a Filament Wound Ring Specimen with a Hole

Eivind Hugaas *, Nils Petter Vedvik and Andreas T. Echtermeyer

Department of Mechanical and Industrial Engineering, Norwegian University of Science and Technology, 7034 Trondheim, Norway; nils.p.vedvik@ntnu.no (N.P.V.); andreas.echtermeyer@ntnu.no (A.T.E.)
* Correspondence: eivind.hugaas@ntnu.no

Abstract: A progressive FEA mechanical fatigue degradation model for composites was developed and implemented using a UMAT user material subroutine in Abaqus. Numerical results were compared to experimental strain field data from high frequency digital image correlation (DIC) of split disk fatigue testing of pressure vessel cut outs with holes. The model correctly predicted the onset and evolution of damage in the matrix as well as the onset of fiber failure. The model uses progressive failure analysis based on the maximum strain failure criterion, the cycle jump method, and Miner's sum damage accumulation rule. A parameter study on matrix properties was needed to capture the scatter in strain fields observed experimentally by DIC. S-N curve for the matrix material had to be lowered by 0% to 60% to capture the experimental scatter. The onset of local fiber failure had to be described by local S-N curves measured by DIC having 2.5 times greater strain than that of S-N curves found from standard coupon testing.

Keywords: finite element analysis; material models; fatigue; filament winding; digital image correlation

Citation: Hugaas, E.; Vedvik, N.P.; Echtermeyer, A.T. Progressive Fatigue Failure Analysis of a Filament Wound Ring Specimen with a Hole. *J. Compos. Sci.* **2021**, *5*, 251. https://doi.org/10.3390/jcs5090251

Academic Editor: Francesco Tornabene

Received: 16 August 2021
Accepted: 3 September 2021
Published: 18 September 2021

1. Introduction

There is an urgent need for composite pressure vessels that can safely and economically transport hydrogen at 700 bar [1,2]. The technology and design standards exist; however, cost is high due to very strict testing and acceptance requirements [3–5] even at lower pressures. For the acceptance tests, a perfect structure is assumed. However, during a vessel's lifetime, small damages such as a minor impact damage may occur from use. It is currently an unknown how much damage can be tolerated in the vessels due to unknown mechanical fatigue resistance. Damaged vessels are replaced by new ones, which is very costly, especially for large vessels.

Today's pressure vessels have a static strength exceeding the design pressure of 700 bar by a factor of about 2.5 or more as required by the design standards. The factor was also identified by Berro et al. in the OSIRHYS IV project [6]. Uncertainties of the effect of the presence of damage are largely related to mechanical fatigue. Numerical analysis in combination with well-chosen experimental data are the key to better understand how damage and fatigue may affect the mechanical performance and strength [6]. In turn, better numerical models may answer how much wear and damage can be tolerated on in use vessels, avoiding early and costly decommissioning as well as reducing costly testing requirements of new designs

Mechanical fatigue in composites causes complex progressive damage development that sets it apart from more conventional materials such as steel. Progressive failure or damage is defined as damage in the material that occurs over a defined time span. In a tensile test the time span is the loading time and progressive failure in the material typically occurs towards the end of that time span just before the specimen fails. In a fatigue test of a metal, the progressive damage will typically occur towards the very last few cycles as a crack is initiated and propagates. In a composite, however, progressive fatigue damage

looks rather different from a metal. Instead of damage and crack propagation occurring over a very short cycle span towards end of life, mechanical fatigue damage in composites occurs steadily over the whole lifetime, gradually changing the structural behavior and redistributing loads [7]. The dominating mechanism for changing strain fields under fatigue is the development of matrix cracking over time [8–10]. Matrix cracking/matrix damage is seen here in its widest meaning, including cracks in the polymer part of the composite, delamination, and fiber-matrix debonding. Developing matrix cracks change how forces are distributed between the load bearing fibers and cause the strain fields to change. Initiation and propagation of the various forms of matrix cracks is a complex phenomenon.

Traditionally, fatigue of composites has been divided into two segments, high cycle fatigue (HCF) and low cycle fatigue (LCF). The domains of the two are defined by the failure mechanism which dominates in the final rupture of the material in question. HCF is dominated by matrix damage, while LCF by fiber failure [8,11–13]. Notably, a relatively large volume of the material is characterized using this traditional approach. The volume is the typical size of the gauge section of a test specimen of roughly 1000 mm^3. In this study, as will be explained later, fatigue is described locally around a fiber bundle, addressing a volume on the scale of a typical element in a FEA, which can be 0.2 mm^3 or less. When developing a finite element model to describe such local fatigue damage in a component, some highly stressed material (near a defect or geometric stress concentrator) may fail after few cycles as "low cycle fatigue", while material in the lower stressed regions may be in the "high cycle fatigue" domain. As such, a component that catastrophically fails after many cycles fails globally in the HCF domain, but it may have local material that also fails in the LCF domain. A FEA material model addressing local fatigue failure has to take local low and high cycle fatigue into account.

High and low cycle fatigue is, however, defined for the composite material, while the FEA model in this study considers fibers and matrix by themselves, though with some interaction effects. Since the matrix is much weaker and traditionally degrades faster due to fatigue than the fiber (higher slope of the S-N curve [14]), local matrix degradation will naturally dominate in the global high cycle fatigue range. Local fiber failure will be prevalent in the low cycle fatigue range. This study focuses on modeling a global high cycle fatigue experiment.

When using finite element models to model matrix cracking, both initiation and propagation needs to be predicted, including the propagation direction. Recent developments in such models have managed to satisfactorily predict matrix damage dominated fatigue damage propagation in laboratory test specimen having simple geometries and known direction of crack propagation, e.g., Turon [7] and Nixon et al. [15] based on the method suggested by Harper et al. [16]. Attempts to simplify the matrix crack growth by smearing matrix cracking over a larger region and modeling it by plastic behavior were reported for the static case by NASA [17], Flatscher et al. [18], and Gagani et al. [19]. It is, however, difficult to tell whether the plasticity approach matches experiments only for the particular geometry of the specimen investigated or whether it is a general way to model the material. For the static case, Rozylo [20] satisfactorily managed to model crack propagation without predefined crack directions using the cohesive zone modelling approach in combination with a user element subroutine (UEL) with promising results. Still, all of the above-mentioned models are relatively academic and not easy for the average design engineer to implement or to get the correct input data for. The models have been developed with lab experiments in mind and not real designs. In this study, the model was developed with the design engineer in mind and then tested on a complex lab experiment. This study therefore has a somewhat different format than most academic publications covering the topic, having a wider scope and less in detail investigations of the experimental results and modelling. This study would however not have been possible without the past academic literature going in depth in DIC and Abaqus in particular.

There are currently some commercial composite mechanical fatigue numerical frameworks available, most notably FEMFAT [21] and Fe-safe [22]. While the models offer simple

and fast fatigue evaluations, they do not include progressive damage and do fatigue analysis based on a static solution. The models are only tested on simple lab coupon specimen and lack experimental comparisons with local strain fields. Recent developments have expanded a modified smearing approach into mechanical fatigue, most notably by Koch et al. [23]. This takes progressive fatigue damage into account. The inherent discontinuity in the stress/strain relationship upon matrix cracking and fiber failure yields challenges in finite element analysis when attempting to reduce the material stiffness at integration points during a constant load. Koch found that a cycle jump approach with constant properties for each loading cycle had to be applied. Degradation was carried out between the jumps according to the size of the cycle jump. A similar approach is used in this work. While Koch compared the model to global experimental data, this work aims to estimate the local experimental strain data as obtained from digital image correlation monitoring of the modelled test specimen. The discrepancy between local and global properties was most notably highlighted by Sevenois et al. [24]. Sevenois argued that matrix crack initiation and propagation on the local scale happens long before catastrophic failure of typical composite fatigue test specimen. As noted by others [25–27], matrix voids affect the mechanical fatigue properties to a great degree, which was also found in the presented work here. This effect is also present in other similar materials such as concrete, where nanoparticles can be added to fill the voids and reduce microcracking [28]. Matrix voids induce matrix cracking on the micro level. It is essential to establish when matrix cracking is initiated on the local level to estimate fatigue life in a finite element model. However, so far this has not been taken into account and global cycles to failure for the material are used as input for local properties in most mechanical fatigue models. Sevenois also highlighted the scale problem. For example, atomistic bonds break long before any typical matrix crack is initiated in the structure. In engineering terms damage causing changes to the structural behavior on a component level is important. In this work the scale of interest is that of strain field changes observable through standard scale in DIC (digital image correlation). Sevenois also argued that detailed local models and sophisticated failure criteria fall short of modelling anything but a perfect structure. Matrix voids and variations in fiber volume fraction throughout the structure will make the real damage development complex. In this work, all the above has been acknowledged and addressed through parameter studies on matrix material properties. The resolution of the DIC method enables comparison between model and experiment on a very detailed level, taking into account local variations in material properties. For the fiber properties, local material properties were successfully found using a damage calculation method on the DIC data. Good correlation was found between model and experiment using the local fiber properties. The DIC methods used in this study have been elaborated in two articles explaining how to trace progressive failure in composites [29] and how to estimate a local S-N curve using DIC data [30]. DIC has recently been proven to be a valuable tool in estimating material parameters such as the fracture toughness [31] by tracing crack propagation visually. The very direct observation method (visual) and the vast amount of data make DIC a measurement method with huge potential for more exactly estimating and monitoring material parameters. That is, provided that the user has the ability to take advantage of the data using modern data tools.

This study suggests a simplified modeling approach that could be sufficient for understanding how local strain fields develop under fatigue loading in the composite material and how this may affect the global behavior. The modelling approach was implemented as a combination of cohesive surfaces and UMAT (user material subroutine) in Abaqus. A few simplifying methods were used:

i. Micro matrix failures were modeled using a continuum damage approach as changes in the stiffness matrix without directionality of the cracks.
ii. Macro (visible) matrix failures were modeled as discrete cracks permitted to propagate along predefined surfaces when certain strain states are met. They were used for through-the-thickness cracks in a ply and for delamination. Only selected macro cracks were modelled.

iii. Discontinuities in the stiffness due to crack growth were modeled using an on and off loading approach in combination with simplified cycle jumping [15,16].
iv. A range of polymer matrix properties were modeled to investigate the natural variations of material properties.

2. Experimental Setup

1 outlines the experimental split disk setup with vital dimensions included. The two holes, located at both sides of the disk, were designed to simulate extreme damage in the composite, and a tension-tension load control fatigue loading with an R-ratio of 0.1 was imposed.

The test rings were cut from filament wound specimen with a layup of hoop/axial/hoop/axial fibers as seen in cut A of Figure 1. The fiber orientation angles were $[\pm 89^\circ_2, \pm 15^\circ_1, \pm 89^\circ_2, \pm 15^\circ_1]$, typical for filament wound pressure vessels [6]. Figure 2 shows winding of the first axial layer. The fibers were HiPerTex W2020 glass fibers from 3B [32] and the resin was Epikote MGS RIMR 135 mixed with curing agent Epikure RIMH 137 [33]. The thickness of each layer was found through microscopy of the cross sections and is described in Figure 1. The holes were cut with a composite specific milling tool; 40200-HEMI produced by Seco Tools.

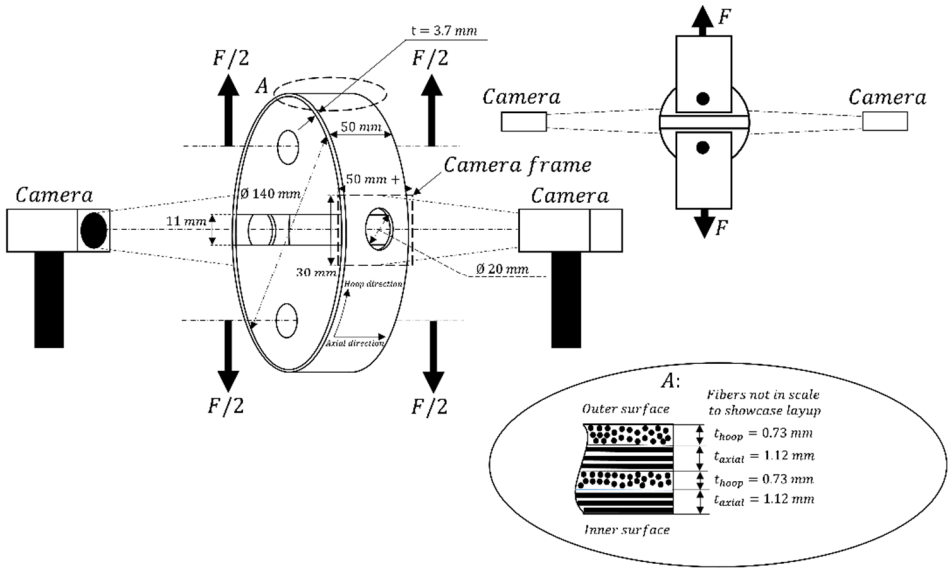

Figure 1. Experimental setup with geometry of test sample and layup; fibers not to scale.

Figure 2. Winding of the first axial layer of the pressure vessel.

Figure 3 shows the test setup in the laboratory. The cameras were timed against the load signal and images were taken at peak load with a frequency of 50 cycles between each image. The DIC data were post processed using Vic-2D from Correlated Solutions. Python scripts developed by the composite group at NTNU were used for extracting results and

performing data analysis. The resolution of the processed data was 4 points per mm^2. Adequate resolution was found through a sensitivity study trying several different resolutions.

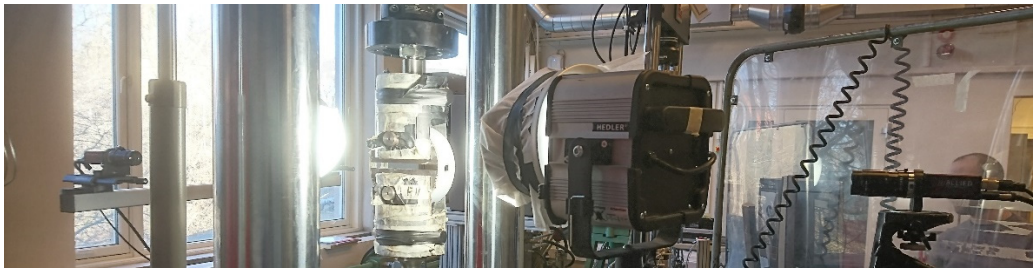

Figure 3. Cameras and test rig with specimen installed. High intensity light was used to accommodate the short shutter speed.

3. Failure Criteria

3.1. General Approach

Failure criteria predict the onset of defined failure mechanisms. Once a state variable (here strain) in the material reaches the limit set by the failure criterion, the constitutive properties are degraded. The scale at which the failure criteria apply also needs to be defined. The scale on which the criteria operate can range from that of the component (load displacement curve from a test machine) and down to the atomistic level. A finite element analysis as used in this study typically represents the mesoscale.

This section describes the failure mechanisms and failure criteria used on the different scales and how the changes in properties are reflected in the constitutive relations. The following failure mechanisms were modeled:

i. Micro fiber failure
ii. Micro matrix cracking (tensile and shear)
iii. Macro matrix cracking (shear failure)
iv. Macro Delamination

An UMAT material model handled the micro failure criteria inside the elements. Macro failures were modeled by a cohesive surface contact definition in Abaqus assuming that the plane of possible failure is known in advance. Figure 4 illustrates the domains of the two methods. Additionally shown are typical imperfections in a ply and sub-categories of micro and macro failure.

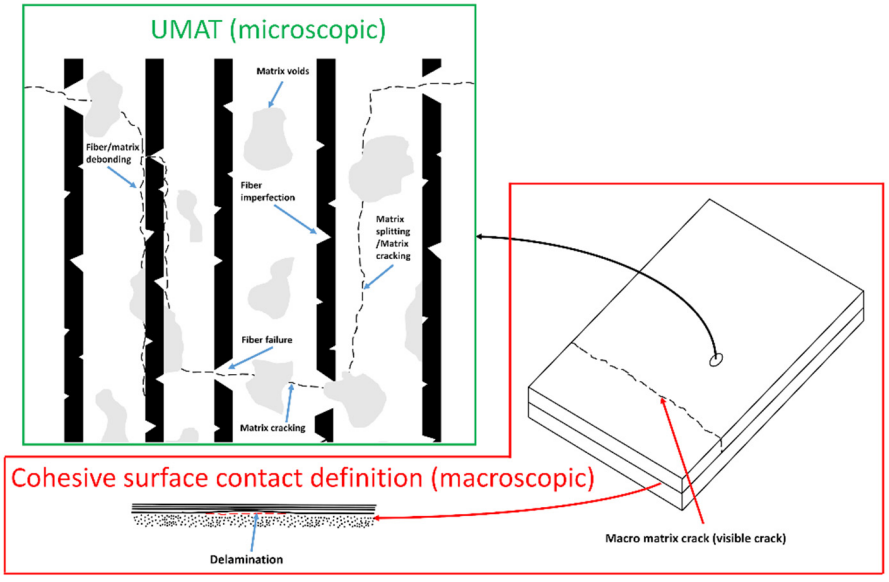

Figure 4. Overview of the failure mechanisms and which modelling method covers which mechanism.

3.2. Modelling Micro Damage with UMAT

Mechanical fatigue was described by a strain-based S-N curve in the log-log format, Equation (1):

$$\log\left(\hat{\varepsilon}_{ij}^{N}\right) = \log\left(\hat{\varepsilon}_{ij}^{O}\right) - \alpha_{ij}\log(N) \tag{1}$$

where $\hat{\varepsilon}_{ij}^{O}$ and α_{ij} are the intercept and slope of the S-N curve respectively and subscript ij denotes the strain components as defined in Figure 5. The number of cycles to failure N_{fail} was defined as in Equation (2):

$$N_{fail} = \begin{cases} \left(\frac{\hat{\varepsilon}_{ij}^{O}}{\varepsilon_{ij}^{N}}\right)^{\frac{1}{\alpha_{ij}}} \text{for } \varepsilon_{ij} < \hat{\varepsilon}_{ij} \\ 1 \text{ for } \varepsilon_{ij} \geq \hat{\varepsilon}_{ij} \end{cases} \tag{2}$$

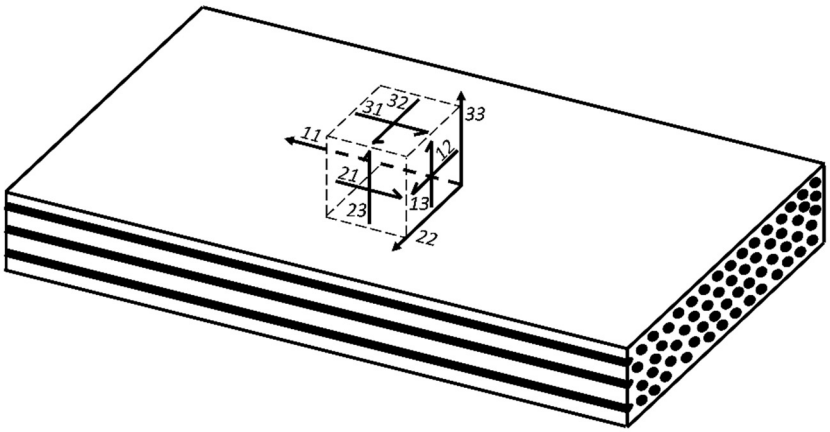

Figure 5. Definition of material directions/components.

If the static strain to failure $\hat{\varepsilon}_{ij}$ was less than $\hat{\varepsilon}_{ij}^{O}$ a cut-off was added to the S-N curve.

Since the strain field changes with the development of partial damage under cycling, the Miner sum M was used, expressed in Equation (3).

Given k number of loadblocks with N^k cycles in each load block at ε_{ij}^{k} strain in each load block:

$$M_{ij} = \sum_{k=1}^{k} \frac{N^k}{N_{fail}\left(\varepsilon_{ij}^{k}\right)} \tag{3}$$

N^k is the number of cycles at strain ε_{ij}^{k} and $N_{fail}\left(\varepsilon_{ij}^{k}\right)$ is the number of cycles to failure at strain ε_{ij}^{k}. k denotes the strain blocks in the Miner sum calculation. A Miner sum of 1.0 is equivalent to breaching the S-N curve failure envelope.

Instead of only calculating the Miner sum, which is a non-physical number, it was useful to define an exposure factor f_{ij}, see Equation (4). The factor describes the ratio of load to material strength at the applied strain ε_{ij} after a certain strain history described by the Miner sum. Failure happens when $f_{ij} \geq 1$.

$$f_{ij} = \frac{\varepsilon_{ij}}{\varepsilon_{res,ij}} \tag{4}$$

$\varepsilon_{res,ij}$ is Hashins's residual strain [34], expressed in Equation (5). It describes the strain to failure after partial fatigue if the material should fail in the next single cycle. It is a direct consequence of the Miner damage rule given in Equation (3).

$$\varepsilon_{res,ij} = \hat{\varepsilon}_{ij}^{O}\left[1 - M_{ij}\right]^{\alpha_{ij}} = \hat{\varepsilon}_{ij}^{1}\left[1 - \sum_{k=1}^{k} \frac{N^{k}}{N_{fail}\left(\varepsilon_{ij}^{k}\right)}\right]^{\alpha_{ij}} \quad (5)$$

The exposure factor enables the introduction of a partial degradation of the material before the particular failure mechanism has happened.

The exposure factor varies for the different strain components since applicable strains and S-N curves may differ. The full set of exposure factors are given in Equation (6). Note that the matrix dominated strains ε_{22} and ε_{33} are influenced by the strain ε_{11} in the fiber direction due to the Poisson's effect, as follows from Equation (6). The opposite coupling is however neglected since this coupling gives neglectable differences in ε_{11} due to the stiffness difference between longitudinal and transverse direction. As the failure criteria were defined such that failure in one matrix associated component or plane (22, 33, 12, 13, or 23) gives failure in all matrix associated components, the coupling between ε_{22} and ε_{33} was also neglected.

$$\begin{bmatrix} f_{11} \\ f_{22} \\ f_{33} \\ f_{12} \\ f_{13} \\ f_{23} \end{bmatrix} = \begin{bmatrix} \frac{1}{\varepsilon_{res,\,11}} & 0 & 0 & 0 & 0 & 0 \\ \frac{\nu_{12}}{\varepsilon_{res,22}} & \frac{1}{\varepsilon_{res,22}} & 0 & 0 & 0 & 0 \\ \frac{\nu_{13}}{\varepsilon_{res,33}} & 0 & \frac{1}{\varepsilon_{res,33}} & 0 & 0 & 0 \\ 0 & 0 & 0 & \frac{1}{\varepsilon_{res,12}} & 0 & 0 \\ 0 & 0 & 0 & 0 & \frac{1}{\varepsilon_{res,13}} & 0 \\ 0 & 0 & 0 & 0 & 0 & \frac{1}{\varepsilon_{res,23}} \end{bmatrix} * \begin{bmatrix} \varepsilon_{11} \\ \varepsilon_{22} \\ \varepsilon_{33} \\ \varepsilon_{12} \\ \varepsilon_{13} \\ \varepsilon_{23} \end{bmatrix} \quad (6)$$

The consequence of failure is a specific change of the set of orthotropic elastic properties of the ply for each failure mechanism. The elastic properties were changed by stiffness reduction factors S_{ij} as given in Equations (7) and (8a,b).

$$\begin{bmatrix} E_{11} \\ E_{22} \\ E_{33} \\ G_{12} \\ G_{13} \\ G_{23} \end{bmatrix} = \begin{bmatrix} S_{11} & 0 & 0 & 0. & 0 & 0 \\ 0 & S_{22} & 0 & 0 & 0 & 0 \\ 0 & 0 & S_{33} & 0 & 0 & 0 \\ 0 & 0 & 0 & S_{12} & 0 & 0 \\ 0 & 0 & 0 & 0 & S_{13} & 0 \\ 0 & 0 & 0 & 0 & 0 & S_{23} \end{bmatrix} * \begin{bmatrix} E_{11} \\ E_{22} \\ E_{33} \\ G_{12} \\ G_{13} \\ G_{23} \end{bmatrix} \quad (7)$$

$$\begin{bmatrix} \nu_{12} \\ \nu_{13} \\ \nu_{23} \end{bmatrix} = \begin{bmatrix} S_{12} & 0 & 0 \\ 0 & S_{13} & 0 \\ 0 & 0 & S_{23} \end{bmatrix} * \begin{bmatrix} \nu_{12} \\ \nu_{13} \\ \nu_{23} \end{bmatrix} \quad (8a)$$

$$\nu_{21} = \frac{E_{22}}{E_{11}} * \nu_{12},\ \nu_{31}\,\nu_{31} = \frac{E_{33}}{E_{11}} * \nu_{13},\ \nu_{32}\,\nu_{32} = \frac{E_{33}}{E_{22}} * \nu_{23} \quad (8b)$$

The Young´s and shear moduli are denoted E_{ij} and G_{ij} and the Poisson´s ratios are ν_{ij}. How the stiffness reduction factors were changed is described in Table 1. The choices behind the factors and their interaction will be explained below.

Table 1. How reduction factors are changed depending on failure criterion.

	S_{11}	S_{22}	S_{33}	S_{12}	S_{13}	S_{23}
Fiber failure ($f_{11} > 1.0$)	0.1	0.1	0.1	0.1	0.1	0.1
Matrix failure ($f_{22}, f_{33}, f_{12}, f_{13}$ or $f_{23} > 1.0$)	0.9	0.1	0.1	0.1	0.1	0.1

As can be seen in Table 1, the factors changed the stiffness extensively, from full stiffness to 10% stiffness. To ease the change, the stiffness was gradually reduced from the intact to the failed value over an exposure factor span from 0.8 to 1.0, as expressed in Equation (9). This is schematically shown in Figure 6 for a reduction from 1.0 to 0.1. Particularly for elements with an exposure factor fluctuating about 1.0, the softening eases the iterative scheme, avoiding distorted elements with a large internal stiffness difference. The largest exposure factor of components 22, 33, 12, 13, and 23 was used as basis for reducing the constitutive properties in these components, in accordance with Table 1.

$$\begin{gathered} \text{if all } f_{ij} \leq 0.8 \text{ then } S_{ij} = 1.0 \\ \text{for largest } f_{22-23} : 0.8 \leq f_{22-23} \leq 1.0 \text{ then } S_{22-23} = 4.6 - 4.5 f_{ij} \text{ and } S_{11} = 1.4 - 0.5 f_{11} \\ \text{if } f_{11} : 0.8 \leq f_{11} \leq 1.0 \text{ then } S_{11-23} = 4.6 - 4.5 f_{ij} \\ \text{if any } f_{22-23} \geq 1.0 \text{ then } S_{22-23} = 0.1 \text{ and } S_{11} = 0.9 \end{gathered} \tag{9}$$

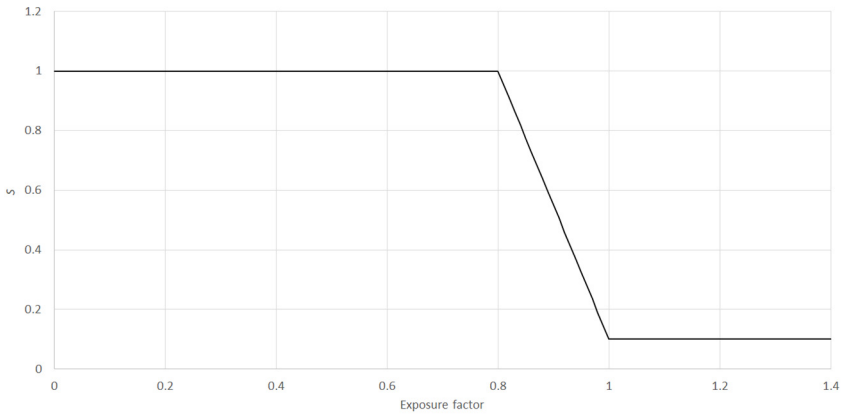

Figure 6. Schematic showing the change of stiffness with exposure factor.

3.3. Modeling Macro Damage with Abaqus Contact Definitions

Delaminations and macro shear cracks penetrating the entire thickness of a ply were described as macro damage, see Figure 4. Delaminations may occur between all the layers. The layers were therefore modeled separately with Abaqus' cohesive surface contact defined on the interfaces. Macro shear cracks were known to develop and extend at four locations in the test specimen. They initiated at the equator of the hole and extended in the loading (hoop) directions along the shear strain bands. Modelling the location of the cracks directly into the FE models significantly simplified the modeling approach.

Abaqus' cohesive surface definition was used with a triangular traction-separation response, illustrated in Figure 7 with the values from the normal direction (t_n, G_n). The separation is defined in mm between the two surfaces. The triangle is defined by an initial elastic stiffness (K) defined by the characteristic element length as given in Equation (11). Upon reaching the maximum stress (t), the contact stiffness is reduced according to the fracture energy G. The elastic stiffness (K) was defined according to suggestions by Diehl [35]. Diehl found that the contact stiffness in the elastic regime was best described using a factor of 0.05 on the characteristic element length as described in Equation (11). The characteristic length was defined as the mean element length, d, along the shear crack in the finest meshed region of the model, giving a d of 0.255 mm. Based on suggestions by Perillo [36] on the used material, the Benzeggagh-Kenane (BK) mixed mode behavior was used along with an energy mixed mode ratio with a BK exponent of 1.4. While the cohesive surface definition needs a defined crack path (here the ply interfaces and shear bands), it is possible to model fatigue macro cracks independently using cohesive zone modelling, CZM [7]. This approach does, however, demand user defined elements (UEL). While this approach is perhaps a closer representation of reality and would not necessitate pre-definition of the shear cracks and ply interfaces in the model, there are several reasons why this approach could not be used in this study. Primarily it is due to the fact that it is, to the authors' knowledge, only possible to run one user defined script (UEL or

UMAT) at a time in Abaqus. Further, CZM is very computationally expensive and would make the runtime impractical. The basic theory is however the same for CZM and the surface definition, with separation between elements and damaged defined with fracture energy. Rozylo carried out a thorough study on CZM in Abaqus and how it could model progressive cracking in buckling experiments in [20]. Rozylo found that the CZM approach was able to match the experiments well. Despite Rozylo carrying out idealized experiments the strain fields were complex giving promise to the CZM for future work.

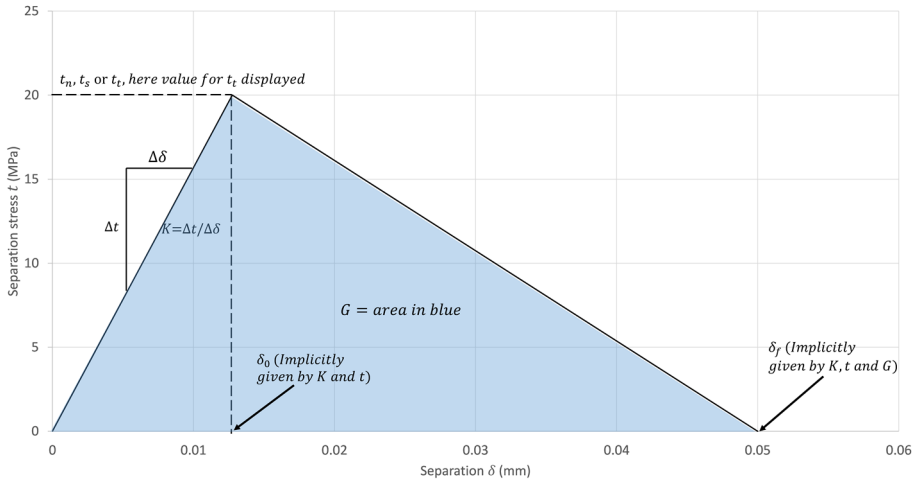

Figure 7. The shape and variables in the traction-separation response. The values on the axis are for the normal component in the traction separation contact definition.

To account for mechanical fatigue in the cohesive surface definition, the contact properties were reduced. The separation stress and the fracture energy were scaled with a factor of 0.6. This factor, 0.6, was chosen based on the graph in Figure 8 showing the S-N curve for the matrix shear with the globally reduced property in red. Details on how the S-N curve was found are given in the Material Properties section. The red line is set close to the convergence of the matrix S-N curve within the cycle span of interest, from 0–100,000 cycles; as the specimen failed at 127,814 cycles. Any strain above this threshold will lead to failure within very few cycles relative to the cycles to failure. The scaling method was done as there is no fatigue definition built into the standard delamination crack definition of Abaqus and it was not possible to the authors' knowledge to run a separate user subroutine on contact properties and micro damage UMAT simultaneously.

$$t_n = \hat{\sigma}_{22T} * 0.6 = 20.0,\ t_s = t_t = \hat{\tau}_{12} * 0.6 = 21.6 \tag{10}$$

$$K_n = \frac{t_n}{d * 0.05},\ K_s = \frac{t_s}{d * 0.05}, K_t = \frac{t_t}{d * 0.05} \quad d = 0.255 \text{ mm} \tag{11}$$

$$G_n = 0.83 * 0.6 = 0.5 \quad G_s = G_t = 3.15 * 0.6 = 1.9 \tag{12}$$

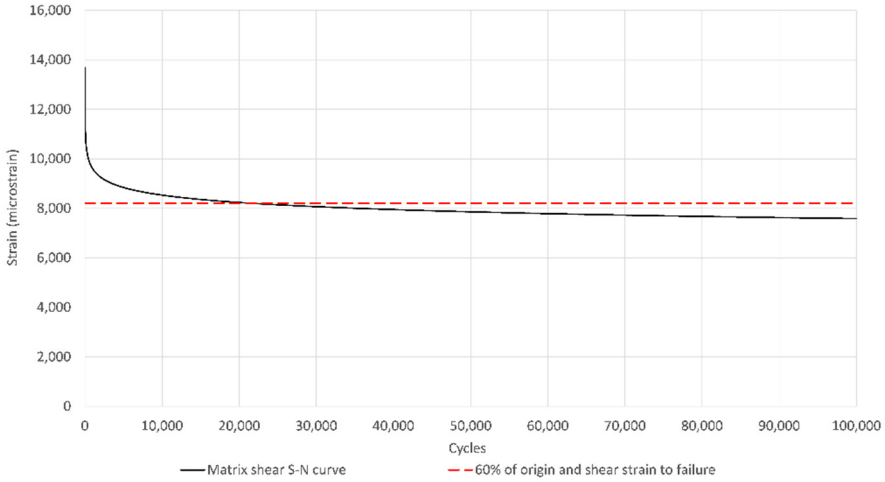

Figure 8. S-N curve for the matrix shear plotted against the reduction factor on the delamination properties. See the Material Properties section for further information on the S-N curve.

4. Cycle Jump Method

4.1. Overview

Fiber and matrix material have little or no yielding once the failure criterion is met. Upon failure they cease to carry the load and the stress-strain curve is discontinuous as a result, shown schematically in Figure 9. The ideal fatigue-degradation material subroutine would iterate the stiffness based on the applied cycles and stress. The local stiffness for each cycle would be decided by a changing and discontinuous stress/strain curve as displayed in Figure 9. As cycles increase, $\hat{}_{\varepsilon}$ and $\hat{}_{\sigma}$ would become lower. Upon reaching $\hat{}_{\varepsilon}$ and $\hat{}_{\sigma}$, the routine would have to be able to handle a negative tangent stiffness. Negative tangent stiffness is in theory impossible using conventional iterative schemes. The fatigue material subroutine outlined above is therefore impossible. The problem was avoided in the presented work by using a cycle jump method, similar to that explored by Harper and Koch [16,23].

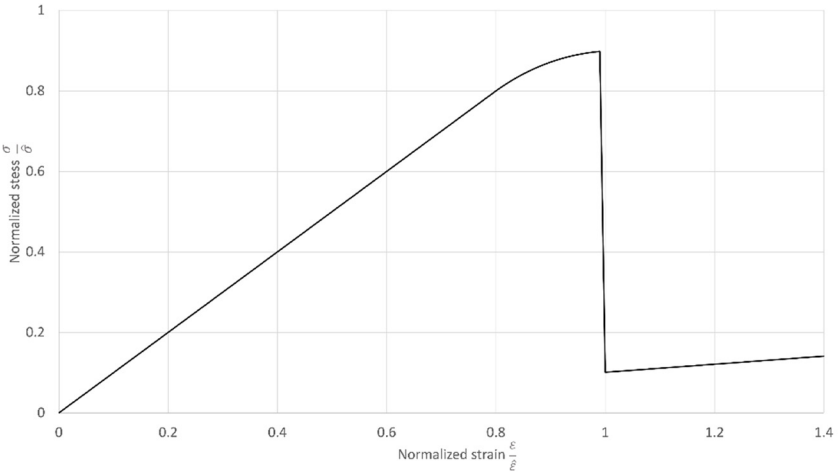

Figure 9. Schematic of a stress/strain curve for a typical fiber or matrix material normalized to the failure stress/strain.

4.2. Implementation

The cycle jump approach has two distinct phases: (i) loading and offloading and (ii) cycle iteration, similar to that explored by Koch [23]. In the loading phase, peak exposure factors and strain in all integration points are recorded. Stiffness is kept constant and not changed as the load is increased to avoid local negative tangent stiffness. When the

peak load is reached, the offloading and cycle iteration phase is initiated. Here the Miner sum is calculated on the peak strains from the loading phase and the exposure factors are changed with cycles. The stiffness is still kept constant in this phase, as the structure offloads to the strain and stress state before loading. Upon initiation of the next loading phase the stiffness is changed according to the new exposure factors from the cycle iteration and the procedure is repeated. In case of simulations with varying fatigue load, this can be achieved by loading to different loads.

Referring to Equations (6)–(8a,b), $\varepsilon^{k}_{res,ij}$ and S_{ij} are kept constant during the loading phase and ε^{k}_{ij} is changed, following the strains in the integration points. During the offloading and cycle iteration phase, ε^{k}_{ij} is kept constant at the peak strains recorded in the loading phase. ε^{k}_{ij} is therefore free from the strain in the integration points and the structure is left to unload by itself. Now $\varepsilon^{k}_{residual,ij}$ is changed according to the cycle in the given iteration. Upon initiation of the next loading phase, S_{ij} is changed according to Equation (9).

Due to the cohesive surface contact definition, the unloading phase may yield singularities in the stiffness matrix. To overcome this, damping was introduced in this phase to have the structure relax without causing singularities.

Figure 10 shows the cycle jump approach explained schematically. The damping is evident in Figure 10 as the displacement curve lags behind the loading curve in the offloading and cycle iteration phase. As the iterative scheme is dependent on the structural response from the damping, the numbers of cycles where results are available in the offloading and cycle iteration phase are not fixed; however, at the end of this phase/step they are. The cycle jumps were chosen based on experimental data in this work.

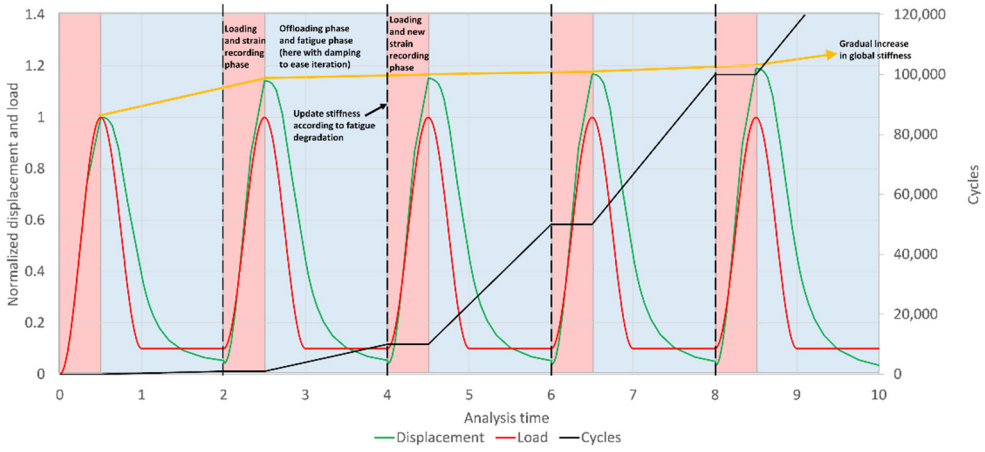

Figure 10. Schematic curves showing how the stiffness changes according to fatigue damage based on the peak strain in each in-tegration point based on the past cycle block.

For complicated models the runtime is long even with high memory and high CPU capacity computers; therefore the cycle jumps has to be placed with care and at critical points in the load history. In most cases this is at the start and end of the component's lifetime. At the start there will be initial matrix cracking and at the end of life there will be extensive fiber failure [37]. In between, the strain distribution will be relatively stable and cycle jumps may be relatively big as a result. Given a load to displacement history from an experiment, it is therefore advisable to place the loading phases at cycles where changes occur in the load to displacement history. Due to the long runtime, it is time consuming to study several different cycle jumps. This study implemented only four well-chosen cycle jumps. Despite this coarse approach, the method gave a good indication of where damage initiated and how this damage affected the strain distribution and material behavior over time. A further expansion of the method would be to include an automatic cycle jump procedure. This could be done by assigning a maximum damaged volume and having

the loading phases occur when damage extends over this specified volume. As such, the method would be completely independent of experimental data. This was done with success by Koch et al. [23] on simple models; however, it was not explored in this work due to the high computational cost. Alternatively, cycle jumps could be set at decreasing intervals until the results of a few cycle jumps converge. This procedure would be easy to implement, but would also require high computational times using a model as big as in this study.

4.3. Material Properties

Material properties of an orthotropic ply with transverse isotropic behavior were used for FEA modeling. A summary of all material properties is given in Table 2. Two main assumptions were made:

i. The plies have transverse isotropic behavior as per classic composite material models.
ii. Only material properties in the tensile direction were considered. The ring on the split disk experienced some compressive stresses. However, since these stresses were small and not in critical regions for the structural integrity, they were not considered and simply modeled with the tensile fatigue data.

Most of the material properties were measured in our laboratory during previous projects from standard coupons made of the same glass fiber and epoxy matrix. Data were obtained for unidirectional flat materials. Filament wound materials have a curvature and are strictly speaking not unidirectional. Properties were scaled to apply to filament wound material using a FEA approach by Perillo et al. [38]. The static properties in the direction of the fiber and matrix (E_{11}, E_{22}, $\hat{\sigma}_{11T}$, $\hat{\sigma}_{11C}$, $\hat{\sigma}_{22T}$, $\hat{\sigma}_{22C}$, $\hat{\tau}_{12}$) were linearly scaled to account for differences in the fiber volume fraction between the filament wound material in this study and that of Perillo.

Table 2 shows the material properties and the methods used to obtain them. Only one static property was measured for this particular study: the maximum static strain to failure of the fibers. Compared to the original maximum static strain found by Perillo of 22,150 microstrain [38], the value reported here of 40,000 microstrain is considerably greater. The value was found from DIC strain measurements taken from static split disk tests [30]. Upon catastrophic failure, 40,000 microstrain was the highest strain recorded. This maximum strain deviated by a margin of almost two from strain at the exact point of failure of 22,150 microstrain, similar to what was found by Perillo from standard coupon testing. The weakest point had similar properties to data obtained by coupon testing, as coupon tests measure the weakest part of the sample. The DIC data showed however that the local strains can be much greater without causing failure. The greatest local strain (40,000 ms) was used for the fatigue analysis.

Fatigue properties were described by strain-based S-N curves for the three in-plane material components of an orthotropic ply: fiber, transverse, and shear components. Figure 11 shows the three individual S-N curves in a linear strain presentation. In all cases the S-N curves could be well described by the log-log presentation as given in Equation (1). All testing was done for an R-ratio of 0.1 (tension-tension). This is the most relevant loading condition for pressure vessels being cycled between nearly empty and full.

Through-the-thickness shear (intralaminar shear) was measured on Short Beam Shear SBS specimen cut from the filament wound vessel with geometry according to the ASTM D2344M standard. The slope of the log-log S-N curve was found by linear regression according to Equation (1). Figure 12 shows the data points and curve fit of the SBS testing. The slope of the curve is 0.051. Nearly the same slope (0.054) was found for the same constituents tested on flat specimens by Gagani [19].

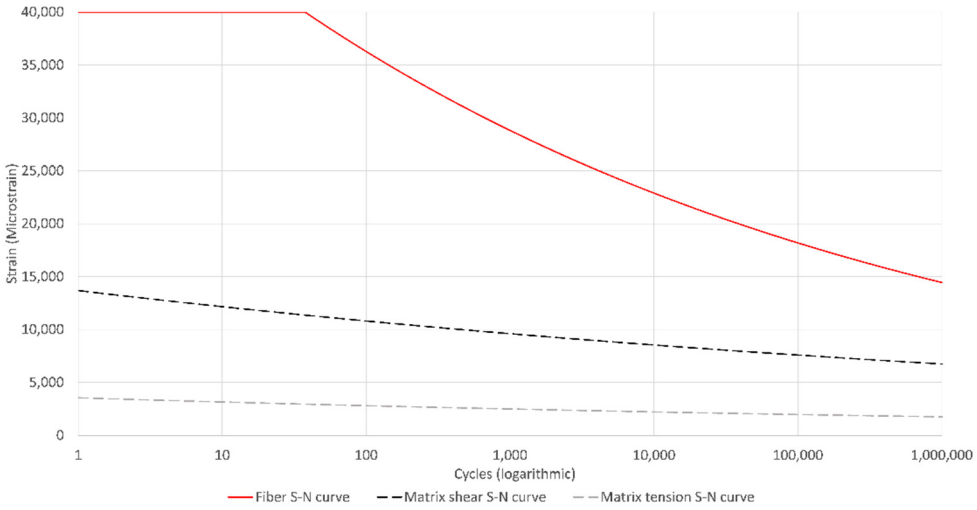

Figure 11. Three S-N curves for the fiber and the matrix directions.

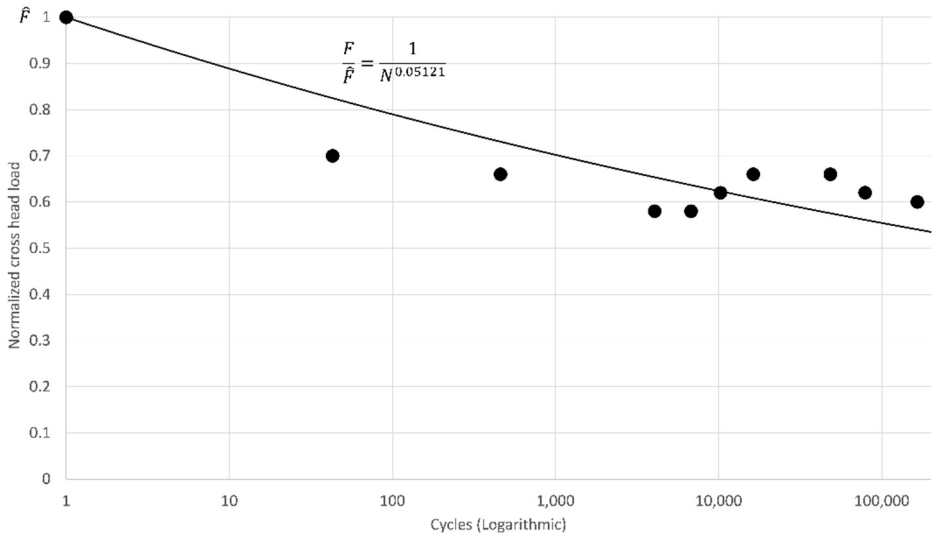

Figure 12. S-N curve for the shear component with data points.

Fatigue properties for in plane matrix cracking were not measured, but taken from the intralaminar shear data. The slope from the shear data was used for the tensile matrix curve with the origin from the static properties. Using the same slope in both tensile and shear S-N curves is controversial; however, it has been shown before that the slope in the tensile matrix direction is in general low [8], as was also found for the shear.

DIC monitoring of the SBS and split disk testing revealed a high discrepancy between local and global fatigue failure and a large scatter in matrix properties. To account for the variations in local properties, a parameter study on the matrix fatigue properties was done and is reported in the Results section, changing the intercept/origin strain of the S-N curves. The parameter study made the exact knowledge of the matrix dominated S-N curves less critical, as the properties were changed in the analysis anyway to capture the experimental scatter.

Local fatigue properties of the fiber were obtained by using DIC data from testing of three split disk ring tests with a hole [30]. Strain based S-N curves were found by an iterative process. Local fiber failures were predicted using Miner sum calculations on the DIC strain data, as in Equations (1)–(3). The predictions were compared with the measured failure of the samples. The S-N curve was changed until a good match between predictions and experiments was achieved. Details of the procedure are given in [30]. The S-N curve giving the best fit with the experimental data had a slope of 0.1, the same as usually

measured for this type of material using standard coupon data [10,11,39–43]. However, the origin of the local S-N curve had to be greater than for typically obtained S-N curves to match the experimental data. The local S-N curve for fiber failure had to be shifted up by about a factor three compared to typically reported curves from coupon testing. This resulted in an intercept of the S-N curve for one cycle that is greater than the static strain found from DIC data, giving a cut-off of 30 cycles on the S-N curve.

Table 2. Material parameters.

Material Parameter	Value	Units	Test Method	Source
		Elastic stiffness properties		
E_{11}	33.06	GPa	ASTM D3039	[38]
E_{22}	9.423	GPa	ASTM D3039	[38]
E_{33}	E_{22}	GPa	Assumption	[38]
G_{12}	2.630	GPa	ASTM D3518/D3518M–13	[38]
G_{13}, G_{23}	G_{12}	GPa	Assumption	[38]
		Static properties		
$\hat{\varepsilon}_{11T}$	40,000	Microstrain	DIC data from static testing [30]	
$\hat{\varepsilon}_{11C}$	354	MPa	ASTM D3410	[38]
$\hat{\varepsilon}_{11C}$	10,725 ($\hat{\sigma}_{11C}/E_{11}$)	Microstrain	ASTM D3410	[38]
$\hat{\sigma}_{22T}$	33.4	MPa	ASTM D3039	[38]
$\hat{\sigma}_{33T}$	$\hat{\sigma}_{22T}$	MPa	Assumption	[38]
$\hat{\varepsilon}_{22T}$	3545 ($\hat{\sigma}_{22T}/E_{22}$)	Microstrain	ASTM D3039	[38]
$\hat{\varepsilon}_{33T}$	$\hat{\varepsilon}_{22T}$		Assumption	[38]
$\hat{\sigma}_{22C}$	96	MPa	ASTM D3410	[38]
$\hat{\sigma}_{33C}$	$\hat{\sigma}_{22C}$		Assumption	[38]
$\hat{\varepsilon}_{22C}$	10,182 ($\hat{\sigma}_{22C}/E_{22}$)	Microstrain	ASTM D3410	[38]
$\hat{\varepsilon}_{33C}$	$\hat{\varepsilon}_{22c}$		Assumption	[38]
$\hat{\tau}_{12}$	36	MPa	ASTM D3518	[38]
$\hat{\tau}_{13}, \hat{\tau}_{23}$	$\hat{\tau}_{12}$		Assumption	[38]
$\hat{\varepsilon}_{12}$	13,681 ($\hat{\tau}_{12}/G_{12}$)	Microstrain	ASTM D3518	[38]
$\hat{\varepsilon}_{13}, \hat{\varepsilon}_{23}$	$\hat{\varepsilon}_{12}$		Assumption	[38]
		Fatigue properties		
$\hat{\varepsilon}^{O}_{11T}$	57,500	Microstrain	DIC data from fatigue testing [30]	
$\hat{\varepsilon}^{O}_{11C}$	$\hat{\varepsilon}^{O}_{11T}$		Simplification	
$\hat{\varepsilon}^{O}_{22T}, \hat{\varepsilon}^{O}_{33T}, \hat{\varepsilon}^{O}_{22C}, \hat{\varepsilon}^{O}_{33C}$	$\hat{\varepsilon}_{22T}$	Microstrain	Simplification and assumption	
$\hat{\varepsilon}^{O}_{12}, \hat{\varepsilon}^{O}_{13}, \hat{\varepsilon}^{O}_{23}$	$\hat{\varepsilon}_{12}$	Microstrain	Simplification and assumption	
α_{11T}	0.1	-	DIC data from fatigue testing	
α_{11C}	α_{11T}	-	Simplification	
α_{12}	0.05121	-	ASTM D2344/D2344M	Figure 12
$\alpha_{22T}, \alpha_{22C}, \alpha_{33C}, \alpha_{33T}, \alpha_{13}, \alpha_{23}$	α_{12}	-	Simplification	
		Cohesive surface contact definition		
t_n	$\hat{\sigma}_{2t} * 0.6$ *= 20.0	MPa	Assumption	[38]
t_s	$\hat{\tau}_{12} * 0.6$ * = 21.6	MPa	Assumption	[38]
t_t	t_s		Assumption	[38]
G_n	$0.83 * 0.6$ *= 0.5	N/mm	ASTM D5528	[38]
$G_s = G_t$	$3.15 * 0.6$ *= 1.9	N/mm	ENF (End Notched Flexure) test [44–46]	[38]

* See section FEA model for factor explanation.

5. Finite Element Model

5.1. Geometry

The composite ring was modelled as a 1/8 model with the geometry in the schematic in Figure 1. The model can be seen in Figure 13. The layers (hoop/axial/hoop/axial) were modelled with five elements thickness each, as can be seen in Figure 14. Each layer was defined through the composite layup function in Abaqus. The layers were defined in this function as 10 $\pm$ layers (+15°, −15°, +15°, . . . , −15° and +89°, −89°, +89°, −89°, . . . , −89°), essentially smearing the properties.

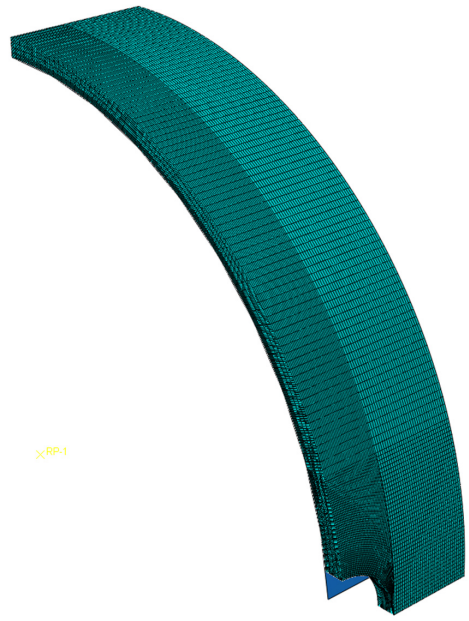

Figure 13. D Model of 1/8 of the split disk. The disk is represented by the rigid surface under the laminate.

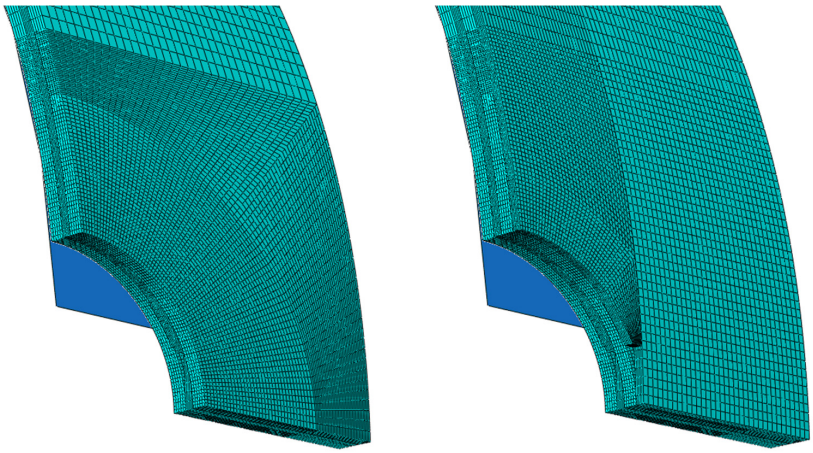

Figure 14. Detail of mesh in split disk model. To the left is from the middle axial layer, to the right is from the upper hoop layer.

The ring was meshed using hexagonal eight node reduced integration elements, C3D8R and had 223,734 elements. As explained in the Failure Criteria section, the layers had a cohesive surface contact definition defined between them to model delamination. The crack (along main shear band) evident in the top hoop layer in Figures 13 and 14 also had the cohesive surface contact definition as explained in the same section. The crack was only present in the hoop layers, while the axial layers were meshed as shown to the left in Figure 14.

5.2. Loads and Constraints

Table 3 gives detailed constraint definitions with reference to Figure 15 for surface name definitions. The cylindrical coordinate system is defined with a radial and a tangential vector.

Table 3. Overview of constraints using normal symmetry.

Surface	Displacement Constraints	Rotational Constraints (Around Axis)
A	Z Local	-
B	T Local	-
C	T Local	-
D	Free	-
E	R Local (with 0.05 friction coefficient in T and Z direction)	-
Center reference point	X, Z Global	X, Z Global

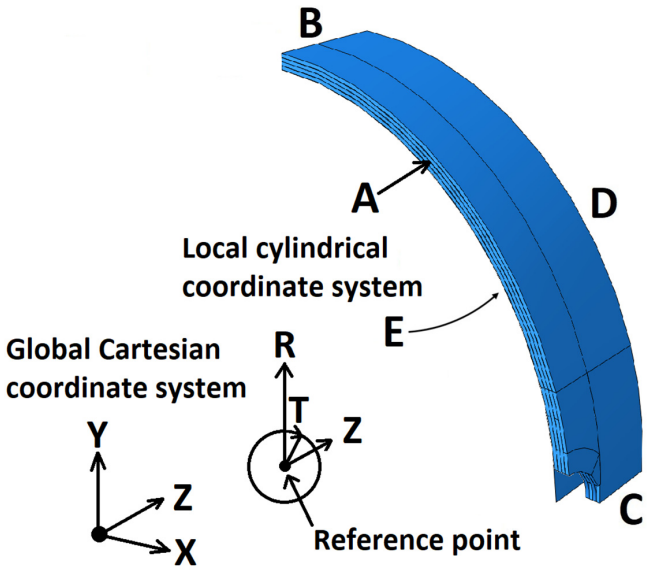

Figure 15. Overview of constraints, surface names, reference point, and the cylindrical coordinate system.

6. Results

6.1. Experimental Results

This study compares experimentally obtained strain fields to FEA modeling of one composite ring with a hole as shown in Figure 1, tested with the split disk test method in fatigue. The strain fields in the vicinity of the hole were measured by DIC every 50 cycles. The sample failed at 127,814 cycles, shortly after the last DIC frame at 127,768 cycles.

Figure 16 shows the cycles to displacement curve from the test machine. The dotted lines are the cycle jumps in the FEA model; these will be further explained in the FEA results section. Catastrophic layer failure/fiber failure in the individual layers happened over relatively short cycle spans indicated by sudden displacement jumps in the curve. The layer failures are highlighted with arrows and text in Figure 16.

There were four regions around the hole in the disk that concentrated strain. The regions are highlighted in Figure 17 over the contour plot of hoop strain close to catastrophic failure. The first fiber failure has already occurred as indicated by the white gap above the black rectangle. The gap was first visible at about 122,000 cycles, roughly 6000 cycles before catastrophic failure of the surface layer. This large fiber failure led to the sudden jumps in the displacement curve visible in Figure 16. It initiated progressive fiber failure

that ripped the layer across the region indicated in the black line slice in Figure 17 before it progressed to the other side of the hole.

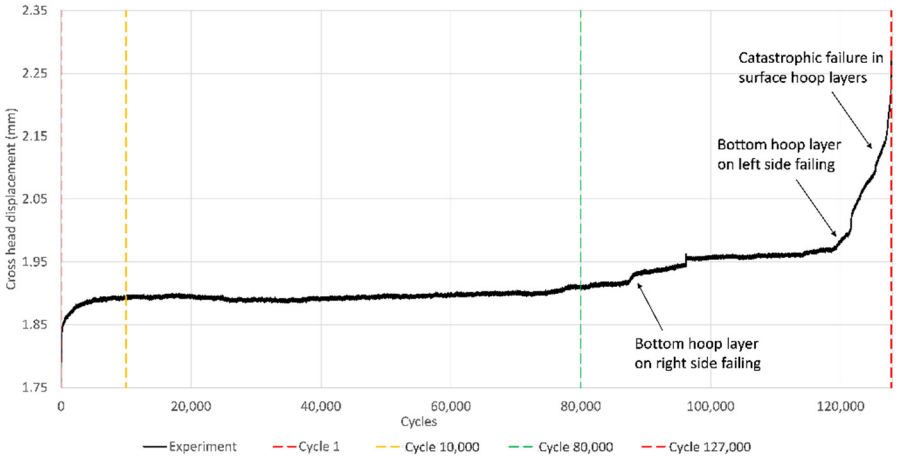

Figure 16. Cycle to displacement curve and cycle jumps.

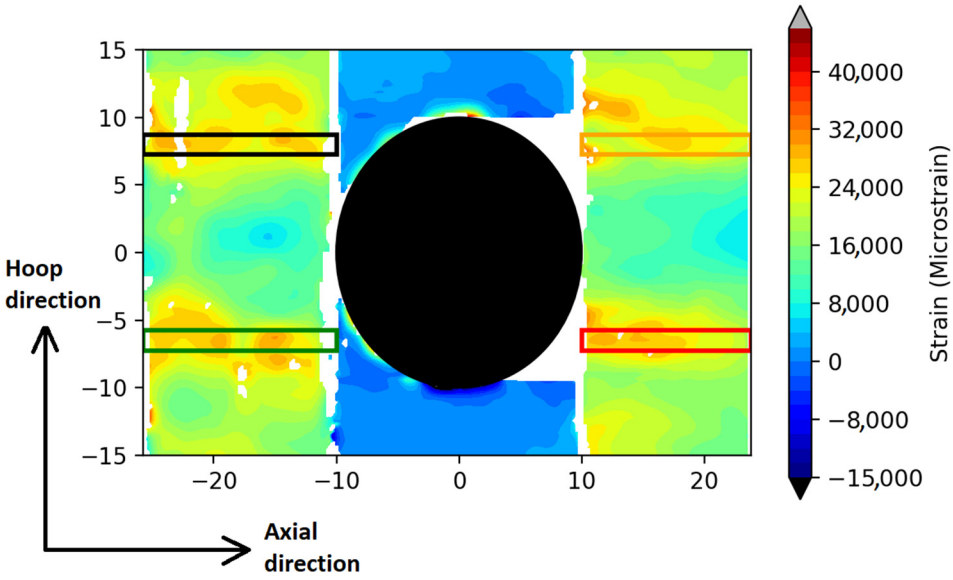

Figure 17. Hoop strain contour plot around the hole at cycle 127,768, shortly before catastrophic failure. The four rectangles highlight the four strain concentrations around the hole.

Intuitively there should be only two regions that concentrate strain, one on each side of the hole at the equator. Macro splits (matrix cracks through the thickness of a ply) develop at these points after very few cycles and the splits grow rapidly in the load direction. The splits and bending of the material between the splits move the strain concentrations to the ends of the splits [47] at the four regions shown in Figure 17.

Provided a perfect material, the four regions around the hole should have equal strain fields throughout the test and equal damage development. Figure 18 shows the strain curves over the length of the four regions at selected numbers of cycles. Cycle 350 was the first recorded cycle by the DIC (cycle 1 was not recorded). The x-axis is in absolute values (note: no negative x values), 10 mm is at the edge of the hole, and 24–26 mm is at the outer edge of the specimen. The curves are evidently not equal. Particularly at cycle 80,000, a factor 1.5–2 difference can be seen between the regions. The differences are due to variations in void content in the matrix, fiber density, and layer thickness; these variations can easily be seen under the microscope, as shown in Figure 19.

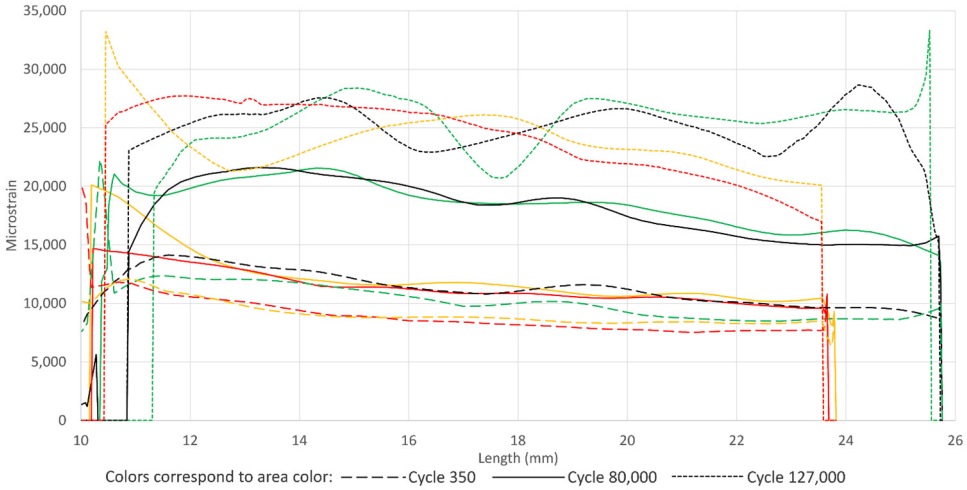

Figure 18. Hoop strain curves from the regions in Figure 17 for different cycles.

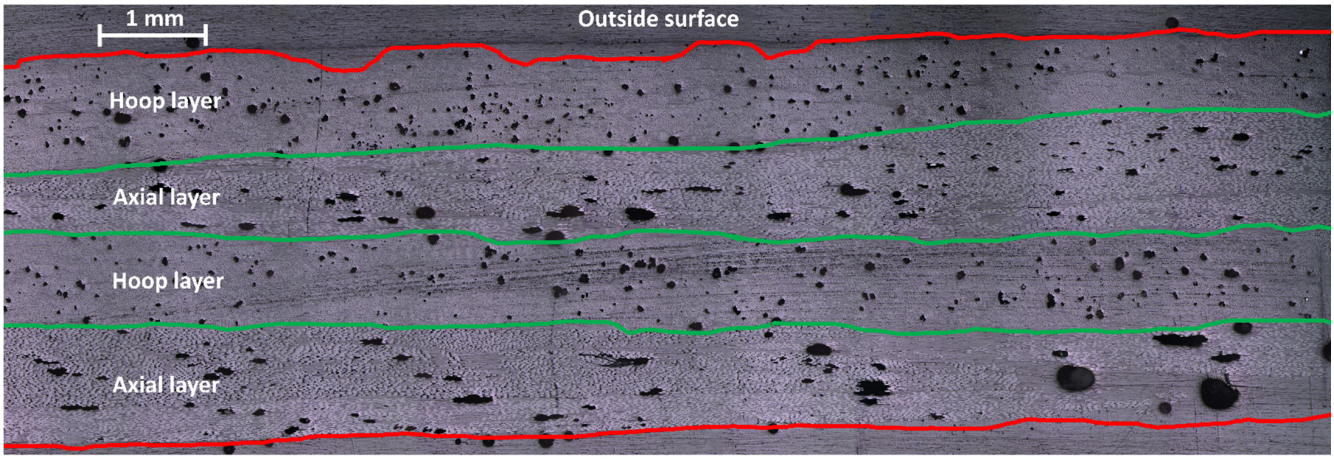

Figure 19. Microscopy of the split disk specimen. As can be seen there are many voids (black) and a big variation in layer thickness over the cross section.

It can be seen in Figure 18 that the strains measured by DIC have a quite pronounced strain concentration at the splits, at the 10 mm position, at a low number of cycles. With increasing number of cycles, the average strain increases but the strain concentration diminishes or moves even to the outer edge of the specimen. This effect is due to matrix damage spreading in the material changing the constitutive properties of the material [29].

6.2. FEA Results

The goal of the FEA modelling was to predict the correct strain field and damage development throughout the fatigue life of the specimen caused by the chosen failure mechanisms using their fatigue failure criteria with corresponding material properties. As shown in Figures 17 and 18 the specimen had big variations in the shape of the experimentally measured strain field over the surface. To capture the variations, the FEA model was run for four cases with different matrix material properties and one case with the failure mechanism in the fiber direction disabled. Tables 4 and 5 show the chosen variations of properties in the models. Model A had nominal properties as defined in the Material Properties section. Models B–D had degradation on matrix properties down to 40% of the original values. In addition, the matrix damage effect on stiffness in the fiber direction was lowered down to 0.7 for the fiber for Model C and D, while Model E had the property degradation in the fiber direction disabled. The properties for the models are a representative selection of a parameter study that explored what correlated best

with the range of experimental results. All models apart from Model A evidently deviate from the assumed physics of the problem, as defined in the Failure Criteria section. It was, however, interesting to explore what degradation was necessary to better capture the experimental results.

Table 4. Parameters for Models A to D for FEA simulations.

	Factor Applied to Nominal Static Values and S-N Curve Origin ($\hat{\varepsilon}^{O}_{22T}$,$\hat{\varepsilon}^{O}_{33T}$,$\hat{\varepsilon}^{O}_{22C}$, $\hat{\varepsilon}^{O}_{33C}$,$\hat{\varepsilon}^{O}_{12}$,$\hat{\varepsilon}^{O}_{13}$, $\hat{\varepsilon}^{O}_{23}$)	**Factor Applied to Contact Strength** (t_n,t_s,t_t)	**Factor Applied to Fracture Energy** (G_n,G_s,G_t)	**Stiffness Degradation Factor of Fiber upon Matrix Failure, S_{11}, see Table 5**
Model A	1.0	$\hat{\sigma}_{22T} * 0.6$	0.6	0.9
Model B	0.6	$\hat{\sigma}_{22T} * 0.6$	0.6	0.9
Model C	0.6	$\hat{\sigma}_{22T} * 0.36$	0.36	0.6
Model D	0.4	$\hat{\sigma}_{22T} * 0.36$	0.36	0.6
Model E	0.6	0.6	0.6	0.7

Table 5. Stiffness reduction factors for Model C, D, and E.

	S_{11}	S_{22}	S_{33}	S_{12}	S_{13}	S_{23}
Fiber failure ($f_{11} > 1.0$)	0.1 (A–D)/1.0 (E)	0.1	0.1	0.1	0.1	0.1
Matrix failure ($f_{22,33,12,13,23} > 1.0$)	0.6 (C and D)/0.7 (E)	0.1	0.1	0.1	0.1	0.1

Variations in layer thickness were not included in this analysis as this is difficult to model correctly, but the effect was modeled indirectly as reduced matrix properties. The shear crack reduction factors were chosen based on the same evaluation as for models A to E.

FEA fatigue calculations were done using the cycle jump method as described previously. Figure 16 shows the cycle jumps over the cycle to displacement curve. The jumps were placed at interesting points in the cycle to displacement curve. Fiber/layer failure manifests itself as displacement jumps in the experimental curve. An increasing amount of matrix failure is expressed as the gradual increase in displacement between the fiber/layer failures particularly prominent over the first 10,000 cycles. The analysis cycle jumps were put before or at critical changes to the displacement curve. The cycle 1 jump is there to estimate the initial state, the cycle 10,000 jump to capture the initial matrix damage, the cycle 80,000 jump to capture the state just before first layer/fiber failure, and the cycle 127,000 jump to capture the state just before catastrophic failure at 127,814 cycles.

Ideally, more cycle jumps should be put between 80,000 and 127,000 cycles, considering the relatively big increase in the displacement. Due to analysis time this was, however, not feasible. The analysis time for one set of material parameters was six days on a fast 8 slot 64 GB RAM computer with an Intel Xeon W-2155 3.3 GHz CPU.

An example for comparing hoop strain fields calculated by the FEA with measured DIC data is shown in Figure 20 for Model D at 80,000 cycles. The most highly strained regions are qualitatively similar. However, the absolute values only match at a few locations. This is to be expected since the experimental data show quite high variations in the four sectors around the hole. The FE model produces the same results in each sector due to assumed symmetries.

Running the FE analysis for each matrix cracking material model described in Tables 4 and 5 allowed comparing the FEA against experimental data for different matrix properties. Figures 21–24 show the lowest and highest experimental strain across the most highly strained cross sections outlined in Figure 18 compared to the experimental results for the four models A, B, C, D, and E for cycle 1, 10,000, 80,000, and 127,000 respectively. The full colored curves correspond to colors of the regions in Figure 17. There is generally good agreement between experimental data and FEA calculated strains for all but the

127,000th cycle. The models fall between the extremes from the experiment for the 1st, 10,000th, and 80,000th cycle. This shows that the chosen matrix material models represent the various degrees of random material variations of the matrix properties fairly well.

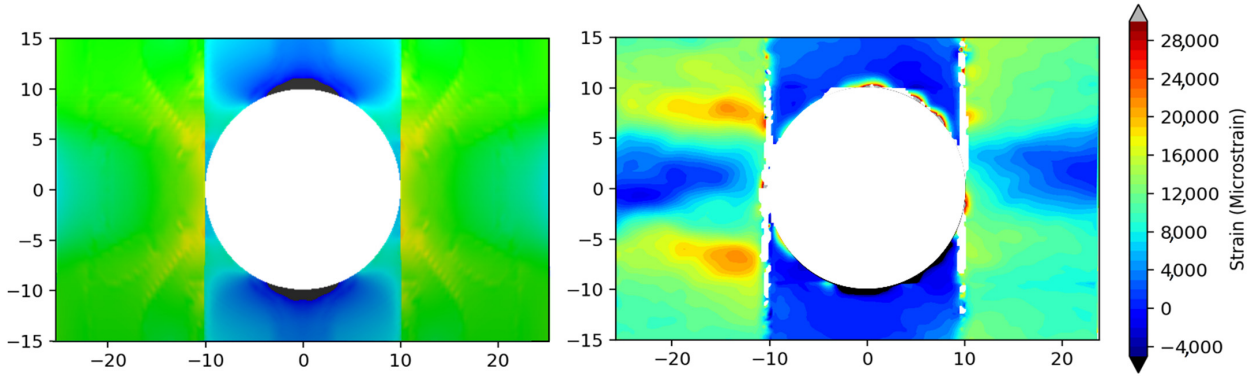

Figure 20. Hoop strain contour plot of FEA Model D at 80,000 cycles (left) compared to the experimentally measured strain (right). The color scale for the strains is the same in both plots. Both plots are for the outer ply.

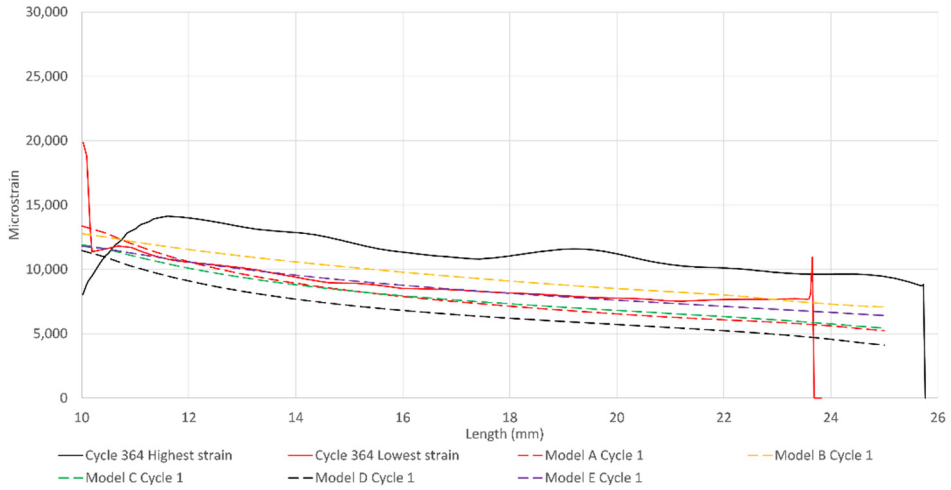

Figure 21. Lowest and highest hoop strain at cycle 364 from Figure 18 compared to the analysis results at cycle 1.

While the low strain curve from the experiment is relatively smooth throughout cycling (Figures 21–24), the high strain curve is not. The high strain curve has also got considerably greater mean strain. The strain curves when using matrix crack models C and D can be seen to have the same uneven shape and also a greater mean strain. The unevenness and greater magnitude are due to more matrix damage. It is interesting to see that the modeled strains start to fluctuate for the highly degraded matrix properties, even though the model treats the properties as the same throughout the model. The black curve in Figure 18 has the same tendency, which is the curve from the region with first observed fiber failure and also catastrophic failure. While the matrix properties are well described using the chosen envelope of degradation in models A–D, it is evident from the 127,000 cycle curves in Figure 24 that strain fields after the bottom hoop layer failure are not as well described as when predominantly matrix damage is present as for cycles 1–80,000. The experimental strains are about 40% greater than the simulated strains after first experimental layer failure. Model D can also be seen to have a substantial fiber failure at 127,000 cycles, which the other models do not have. It is, however, not consistent with where the experimental fiber failure occurred, which was at about 22 mm along the length axis in Figure 24, as commented in the Experimental Results section. The fact that the fiber failure location deviated from the experimental results was the main motivation for

disabling the fiber failure degradation in Model E. Additionally, the drastic stiffness change of fiber failure caused an extensive runtime for Model D.

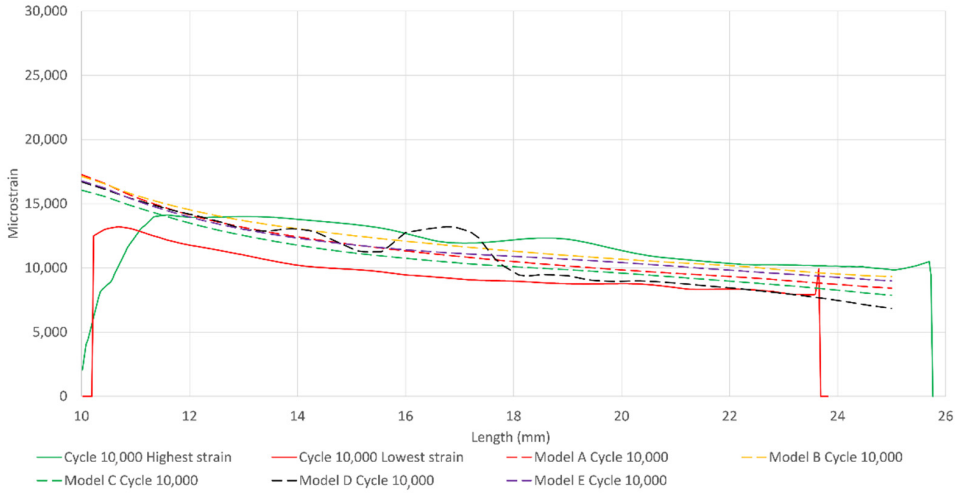

Figure 22. Lowest and highest hoop strain at 10,000 cycles from Figure 18 compared to the analysis results.

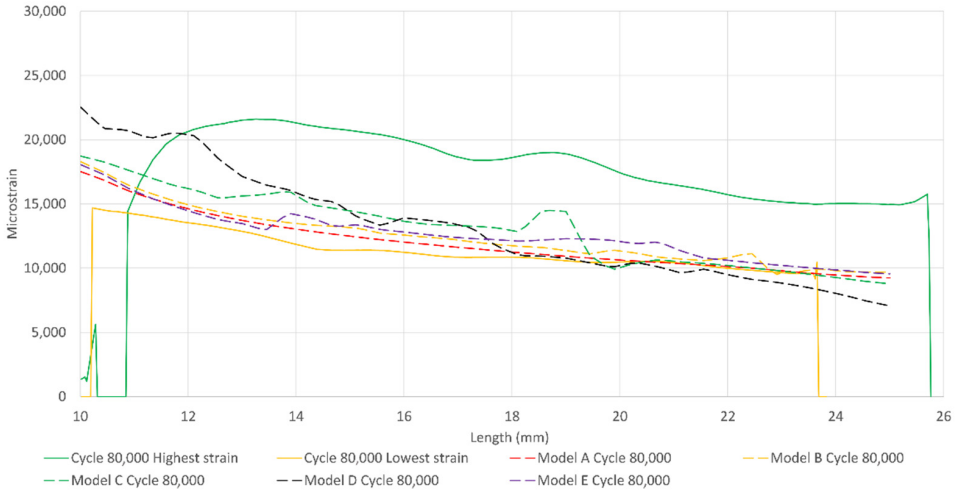

Figure 23. Lowest and highest hoop strain at 80,000 cycles from Figure 18 compared to the analysis results.

Figure 25 shows the peak exposure factor for the 22, 33, 12, 13, and 23 (matrix) components for the outer ply. The maximum was in all cases in the 22 direction. There is a region to the right of the hole at the split with a high exposure factor, corresponding with the high experimental hoop strain region in Figures 21–24. As can be seen, models A–E predict an increasing amount of matrix damage. It can be seen that the degree of strain fluctuations in the model's hoop strain graphs corresponds to the degree of matrix damage.

The FEA calculations for the onset of fiber failure (first recorded fiber exposure factor above 1.0 in any integration point) are shown in Table 6, from Equation (6). Initial fiber failure was predicted to happen in the inner hoop layer in all cases, same as in the experiment. For Model A and B it was predicted at the equator of the hole, while for models C–E it occurred at the end of the splits. The table and cycle numbers will later be discussed and suggested as design criteria.

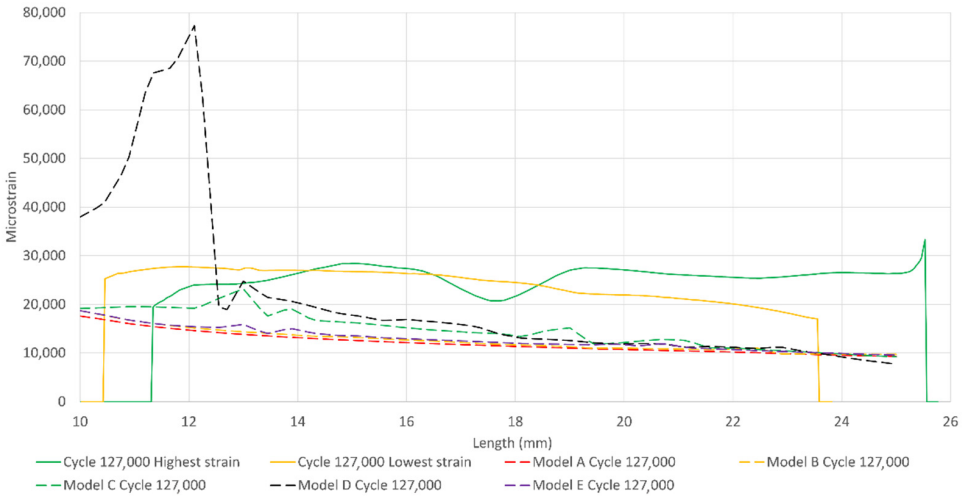

Figure 24. Lowest and highest hoop strain at 127,000 cycles from Figure 18 compared to the analysis results.

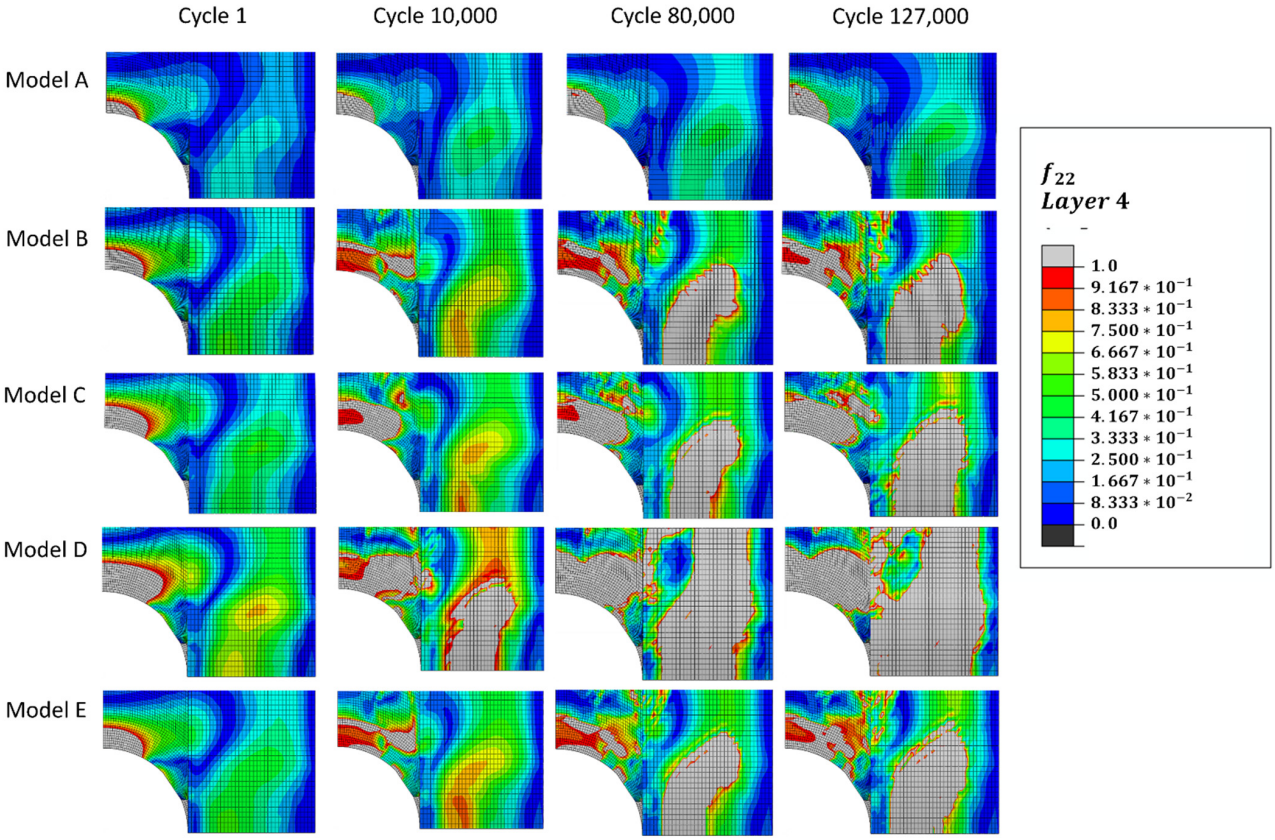

Figure 25. Exposure factor for matrix dominated fatigue failure (22 component of the surface ply). The scale is from 0 to 1.

Figure 26 shows the FEA calculated exposure factor in the fiber direction for model A, D, and E at 80,000 cycles for the bottom hoop layer. While Model A has relatively little damage in the fiber direction, Model D can be seen to have extensive damage, nearly half the load bearing cross section of the layer has an exposure factor above 1.0. Model E falls in between the two others. Model B and C are not shown; these were also in between A and D in damage extent. Catastrophic failure of the ring happened at 127,814 cycles. At that number of cycles the FEA predicted strains were lower than the experimental strains, as described above, so the accuracy of the FEA model was not too good anymore. This is

evidently due to the fact that catastrophic failure of the bottom hoop layer in the model is very difficult to model correctly. Any exposure factor evaluation in top hoop layer is there for difficult to evaluate and will not be presented.

Table 6. First fiber failure in models A–D.

Model	Onset of Fiber Failure	Location
Model A	19,930 cycles	Hole equator
Model B	19,930 cycles	Hole equator
Model C	16,390 cycles	Split
Model D	11,400 cycles	Split
Model E	11,400 cycles	Split

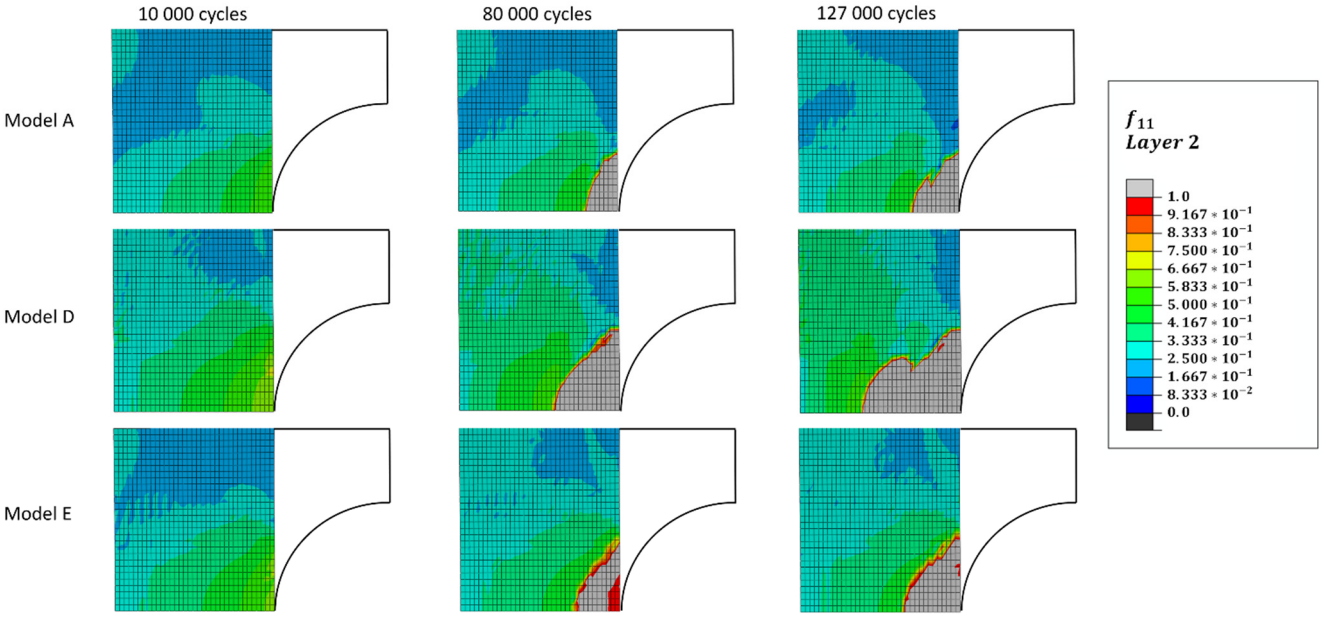

Figure 26. Exposure factor in the fiber direction of the bottom hoop layer at 80,000 cycles. Only one side of the shear crack is shown as damage developed there.

While the strain plots give a good overview of the local behavior of the ring specimen, the displacement curve gives a good indication of how changes to the local stiffness affect the global behavior. Figure 27 shows Models A–E compared to the displacement from the experiment. All models predict a rapid increase in displacement within the first 10,000 cycles. This increase is due to developing matrix damage, making the sample more compliant. The experimental curve shows that this damage develops much faster, mostly within the first cycle. The discrepancy is due to the fact that the cycle 1 step was run without any damage in the FEA analysis. This is different from the experiment, where the cycle 1 loading gave initial matrix damage and evidently greater displacement than the models. The models converge with the experiment after the second step at 10,000 cycles. Putting in more cycle jumps would reduce the discrepancy, but since the focus of this study is not on the short-term behavior, no further investigations of this phase were done.

Further matrix cracking created a gradual increase of displacement for all models. The increase was lowest for model A and highest for model D, as would be expected from the material properties used in the models given in Table 4. The experimental data show a mainly flat curve up to 80,000 cycles and then a gradual increase in displacement. However, within an error of about 10% models A, B, and C match the experimental data, models C and E being the best. Model D gives a much too compliant behavior.

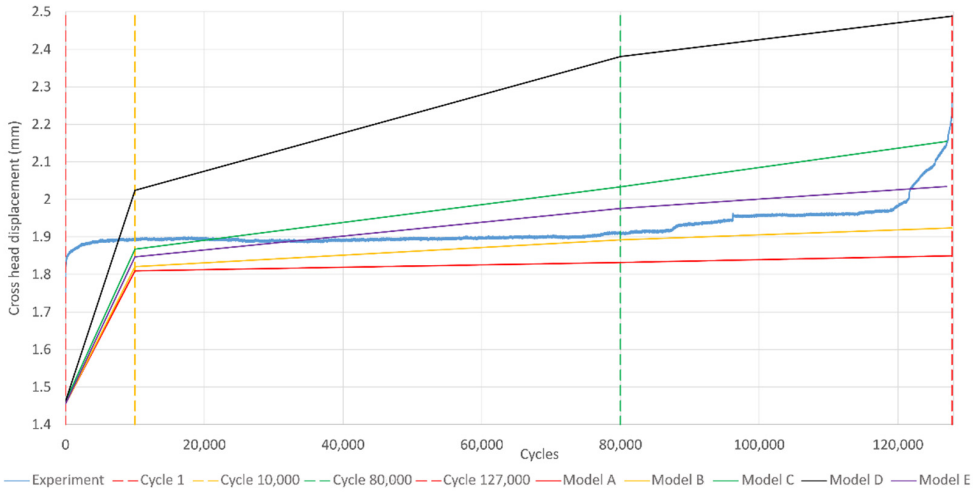

Figure 27. The displacement differential from the experiment and test compared.

The displacement curves show that the models did not properly account for spreading of fiber failure. Displacement increases due to matrix cracking were, however, relatively well described, as evident between 1 to 10,000 cycles. The experimentally observed jumps in the displacement curve due to fiber failure are difficult to capture with such few cycle jumps.

The macro shear crack length is shown in Figure 28. The crack length is defined as the length of the crack where the cohesive parameters $\delta_0/t_n/t_t/t_s$ in Figure 7 were exceeded. The shear crack length as defined by the gaps in the DIC contour plot (see Figures 17 and 20) is shorter than this, as voids first come when there is a visual shear crack. It can however be seen that shear crack modeled by FEA extended outside the frame of the DIC (15 mm) for all the models at almost all cycles.

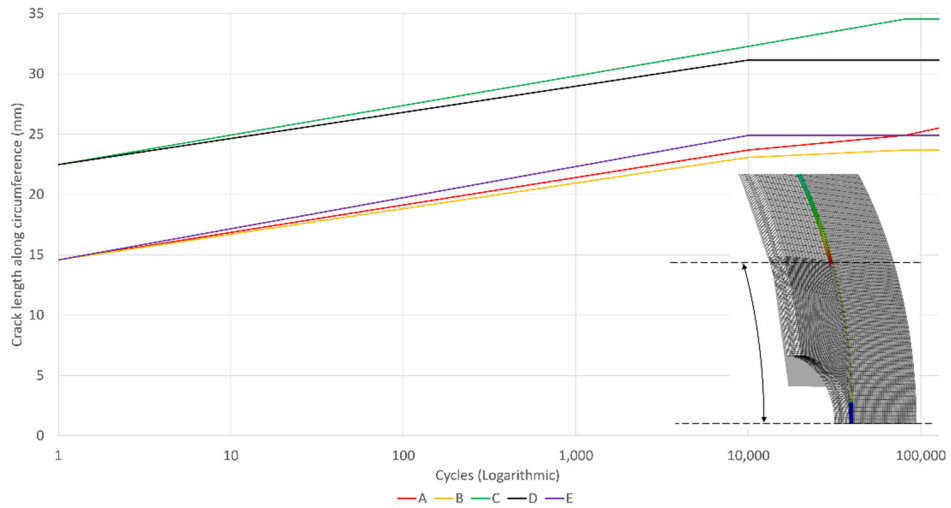

Figure 28. Shear crack length (length that has breached δ_0 in Figure 7) along the circumference of the FEA model.

Delaminations were not measured experimentally except for some visual investigation of the edges of the ring specimen during testing (see Figure 29). The cracks highlighted with red arrows in Figure 29 are evidently macro cracks, but were not included in the model as they have much less effect on the strain distribution in the loadbearing layers compared to cracks in the hoop layers, while also being harder to predict. Figure 30 shows the delaminations in the models between layer 3 and 4, as they were the most extensive. As can be seen, the delaminations differ from the experiment when comparing Figures 29 and 30. The delaminations in

the experiment run through the equator between layer 3 and 4 and are more extensive than in the model. The discrepancy is likely due to the fact that the macro cracks created free edges inside the specimen which delaminations could grow from due to more shear stress in the layer interfaces. The cracks on their own reduced the bending stiffness while also causing delaminations to grow and are the likely reason for the apparent low bending stiffness of the material in the split. The low bending stiffness gives the low strain in the center of the disk in the experiment compared to the model, as shown in Figure 20.

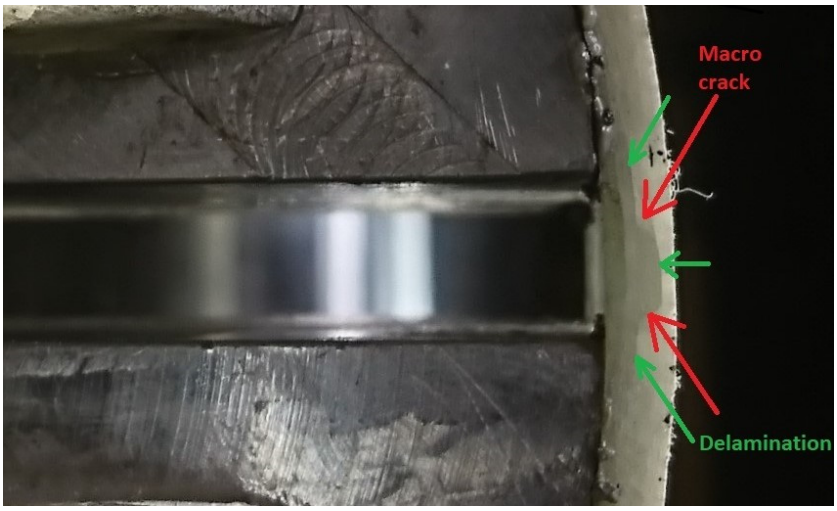

Figure 29. Macro cracks (red arrows) extending through the middle axial layer with delamination on either side of the middle axial layer (green arrows).

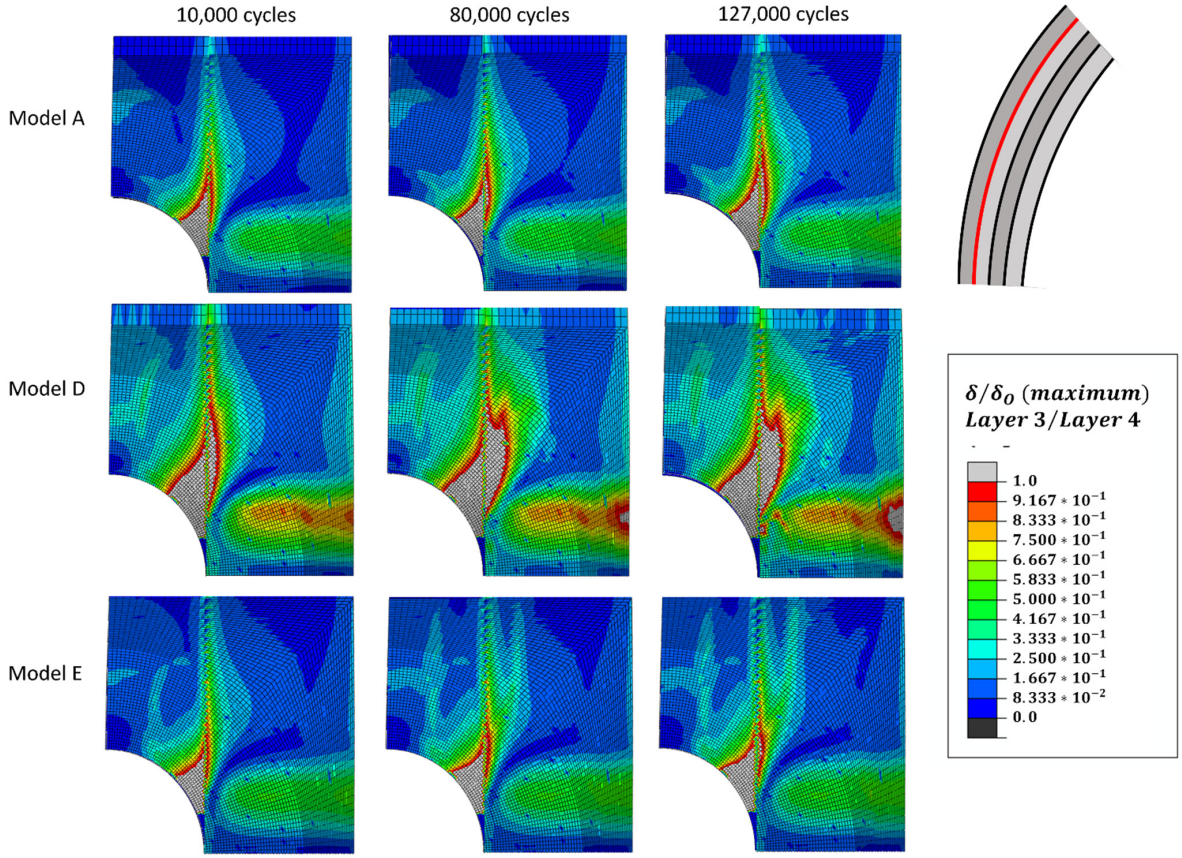

Figure 30. FEA delamination between the most delaminated layers in the model, layer 3 and 4, as indicated in the schematic.

7. Discussion

The experimental strain field measurements performed by high frequency DIC have shown that the local variations in material properties significantly change the strain. Figures 17 and 18 show the differing strains in the highly strained and critical regions. Using simple symmetry arguments, the strains in the four quadrants around the hole of the ring test should be the same for a component with identical material properties.

The local changes in material properties are a result of the production process and natural variations in material properties. Especially for the filament wound material investigated here, local variations in fiber content, fiber placement, and presence of voids are quite pronounced, amplifying these effects compared to better-controlled materials, such as prepregs. However, to some extent these variations are present in all composite materials.

Modeling the random variations of the material´s behavior is a challenge. This work used a simplified approach by modeling the ring specimens several (five) times with a constant set of material properties for each modeling run. The initial matrix properties and their degradation characteristics were changed for the different runs. The high frequency DIC measurements allowed comparing experimental fatigue strains with FEA simulations on a high level of detail.

Looking at up to 80,000 cycles, the comparison showed that the nominal material properties (model A) described the least damaged parts of the specimen well. Model D with degraded properties described the most damaged part of the specimen well. Model B, C, and E were between the two. Modeling the entire specimen with a constant set of matrix properties is not ideal, as it deviates from the real physical conditions, but the agreement between experiments and FEA shows that this simplified approach manages to capture the strain envelope reasonably well. The approach should be sufficient for most practical purposes. Model D was the only model that had enough fiber damage to show on the strain curves, with strains in the fiber direction up to 0.8%. However, the fiber failure occurred at a different spot from the experiment. Seeing as the modeling method did not capture fiber failure correctly, Model E was run without any degradation of fiber failure associated properties and with degradation of matrix properties in between Model D and Model C.

The FEA calculates that the first local fiber failure happens already at 10,000–20,000 cycles for all models. This is the first point in the models with an integration point showing an exposure factor above 1.0 for the fiber direction. Due to the initial matrix cracking phase being more or less the same for all models, the first registered exposure factor above 1.0 falls within a short cycle window. However, as stated above, it was concluded that the method falls short of modelling catastrophic fiber failure correctly. The reason being that the experiment consisted of many strong and weak fibers, while the model treats all fibers the same. Such a drastic event as fiber failure therefore becomes difficult to model correctly due to statistical variations in the experiment. To model it better, some failure criteria that initiate fiber failure when a region of a certain size has an exposure factor above 1.0 may be better. However, this is a computationally expensive approach. The modelling method in Model E may therefore be the most fit for purpose as it gives the user an idea of how big a region may give fiber failure without the added computational cost of modeling the failure (relative to the other models, Model E was computationally faster with less iterations). Knowing when the exposure factor in the fiber direction reaches 1.0 in the model may be a good design input, as it occurs about a decade before catastrophic failure, which gives a reasonable safety factor for design purposes. Most importantly, the modelling gives a good indicator of how the strain fields will develop throughout the fatigue life. As can be seen, the general trend is the same for all models, with a flattening of the strain field with increasing cycles and damage. Considering the material model's poor ability to correctly model the progression of fiber failure, but good capability to model matrix damage, it can be said that it is more fit for modelling components with a high cycle fatigue issue rather than low cycle.

After initial local fiber failure, further local fiber failures develop according to the FEA. As shown in Figure 26, the region with local fiber damage spreads mainly in the

loading/hoop direction along the splits and across the width of the specimen. The first global response from fiber damage between 80,000 and 90,000 cycles, as seen in Figure 16, is due to an accumulation of local fiber failure that can connect via matrix damage to create a more global crack. The current FEA model is not capable of describing the accumulation of fiber damage properly, as element deletion or contact breaching has to be used in addition to stiffness reduction of the elements to properly characterize the failed regions. Such routines are computationally expensive. The FEA model should be accurate up to first fiber failure. Afterwards, the model shows reasonably well what is happening in the ring specimen, but it should be seen more as a qualitative characterization. Model D and E with the weak matrix describe much more fiber damage than models A, B, and C with a stronger matrix, as would be expected.

Catastrophic failure happens at 127,814 cycles; a decade after the first fiber failure was predicted. The progressive development of damage leads to fluctuations in the strain field across the width, both in FEA predictions and in experimental DIC measurements. It seems that these fluctuations indicate the onset of serious fiber damage, damage that leads to a global response of the structure. The first fluctuations were already seen for the C, D, and E models at 80,000 cycles, see Figure 23. The fluctuations are very pronounced at 127,000 cycles, see Figure 24, even though the absolute strain values between experiment and FEA do not agree too well. These fluctuations could potentially be used as a non-destructive evaluation (NDE) method indicating imminent catastrophic failure. Qualitatively it can be observed that local fiber failures develop and spread without causing a recognizable global response. Matrix damage increases in parallel. Once a combination of local fiber damage and sufficient matrix damage exists, the benign local fiber failures can rapidly combine into global fiber damage causing macroscopic/catastrophic failure.

The FEA used here addresses all failure mechanisms and degradation of material properties after failure, creating a full progressive mechanical fatigue analysis. It is based on very simple maximum strain failure criteria and easily obtained material data. Nevertheless, the set of input data needed is large, as shown in Table 2. The good agreement with experimental results up to first fiber failure is an indication that the modeling approach was successful. It is worth looking at some of the simplifications made. All micro failure mechanisms, axial and shear matrix cracking, and local fiber failure, are described by simple non-interacting maximum strain criteria. The scatter in experimental data, especially the large effects of locally varying material properties, dominates the result, making the simple failure criteria adequate. Whether the simple criteria would also work under more complex multiaxial loading conditions is currently unclear and would need further experimental work to find the answer. In principle the cycle jump approach described here can be easily extended to more complex failure criteria if needed.

Another simplification was to prescribe in advance that the dominant shear crack would develop from the equator of the hole in the ring specimen parallel to the load direction in the hoop layers. This simplification reduced the computational effort significantly. For simple and well-defined loading conditions, the position of the shear cracks can be easily estimated in advance and possibly confirmed by simple experiments. The experimentally observed axial cracks were not modeled in advance and subsequently ignored by the FEA. It was argued here that these cracks were not critical for the ring specimens tested. In principle such cracks could be easily added. If the loading directions are completely unknown, the prescribed crack direction can be a severe limitation and the macro shear crack will matter more, as investigated by Turon [7].

The planes in which delaminations would develop were prescribed in the same way as for the shear cracks. This simplification should work well under most loading conditions. However, the method for defining the macro matrix crack and delamination is somewhat in contrast to other studies covering this topic, taking a highly simplified approach. Figure 28 shows the crack length defined through breaching of δ_0 in Figure 7. Compared to the gaps in the strain field in Figure 20 it may appear that the actual shear crack is shorter than the modeled; however, the gaps may appear long after the material has cracked and certainly

long after the elastic regime defined by δ_0 is breached. The gaps simply indicate when the DIC is not able to pick up any displacement in the speckle pattern. The key role of the shear crack from a strain distribution perspective is to hinder transfer of shear strain across the crack line leading to a greater strain at the 10 mm position in the strain graphs in Figures 21–24. The strain at the 10 mm position in the curves in Figures 21–24 varies very little even though the C and D models have a shear crack twice as long as the A and B models. This indicates that for the split disk ring, the shear crack length is not critical for getting the right strain field in the peak strain regions as long as the crack is longer than a certain minimum. This is an attribute of the modeled geometry. In other applications the macro shear crack will matter more, as investigated by Turon [7]. For future work, it could be possible to combine the methods from the UMAT in this work into a UEL with CZM. As demonstrated by Rozylo [20], the CZM approach is robust and able to predict crack paths in complex strain fields. With the cycle jump approach in the UMAT presented here it would be possible to make a UEL that takes into account both macro and micro cracking, making for a very robust progressive fatigue model. The runtime would very likely be an issue; however, simpler models than the one in this study would be sufficient to serve as a proof of concept and with the computers of tomorrow runtime may not be a worry in the future.

Another simplification was the use of the cycle jump method. As found in previous studies, the method seems to work well. The analysis steps were chosen here based on experimental results. It was a convenient way to identify the critical steps, but only possible if experimental data are available. To increase applicability and improve accuracy, a better estimation of cycle jumps would be needed. This could be done by convergence of strain or damage over time by running several models with different cycle jumps. These models could be more coarsely meshed or only contain parts of the full model. More elaborate approaches to estimate cycle jump size and position already exist for simpler models [7,15,23] and should be possible to implement on larger models as well.

It seems a good balance of simplicity of the FEA and accuracy of the results was found for this study. Adding more complexity to the FEA, especially fiber matrix interaction effects and cycle jump iteration schemes, may get closer to the physics of the behavior of the composite, but also increases dramatically the computational effort. Whether a more complex model will improve the results remains to be seen, because usually further uncertain assumptions need to be added on a detailed level. The variation in material properties remains in all cases and requires using a worst-case approach for design calculations at the end.

Traditional design calculations would use S-N curves for fiber dominated failure obtained from coupon tests and apply them to the stress/strain concentration points in the structure. For this material an S-N curve with the origin at 22,150 microstrain [36] would yield very conservative first fiber failure estimates. In this study the highest strain near the hole was around 1.5 to 1.8%. This would lead to 100 to 1000 cycles to failure, far below the actual catastrophic failure. The reason for the mismatch is using an S-N curve describing large catastrophic failure on the scale of a few cm to local non-critical damage development at a stress concentration.

The FEA shown here uses an S-N curve describing local fiber failure taking local material variations of the matrix into account. This curve is more realistic for use in stress/strain fields with large gradients. Since the accuracy of the FEA currently drops after first local fiber failure, a designer could use the first fiber failure for the weak material D as a design criterion. The predicted cycles to failure are then 10,000, which are much more than predicted by the traditional method. It should still be a reliable approach, because the FEA is fully capable of reproducing local strain fields. This approach is basically designing for first ply failure, a method widely used for static analysis. The approach has been applied before in the FADAS mechanical fatigue model for simple test coupons by Passipoularidis et al. [48]. The FEA can be used further to estimate the location of final

catastrophic failure and it could indicate how the strain fluctuations would look that would develop as a warning before catastrophic failure.

8. Conclusions

A finite element analysis (FEA) material model describing mechanical fatigue of composites by a progressive degradation model using the cycle jump method was developed. It is aimed at pressure vessel applications and focuses on fatigue behavior under tensile load cases, such as that found in industrial pressure vessels. It uses typical failure criteria for transversely orthotropic materials and degrades the stiffness in each material direction based on the Miner sum damage calculation with log-log S-N curves. The model is relatively simple and requires only the typical input parameters used for composite laminate analysis.

Strain fields from FEA were compared with DIC strain fields from split disk testing of a composite ring specimen. Extensive variations in damage development and strain fields were measured by DIC over the specimen due to variations in void content, layer thickness, and fiber volume fraction. The strain in the four regions around the split disk hole varied with a factor of 1.5 to 2 at the most over the course of cycling. To address the variations, the FEA model was run with a parameter study on matrix properties. The most damaged regions (with strain 1.5 to 2 times higher than the least damaged) were best modeled by using S-N curves for matrix properties degraded by 40% compared to the original values. The original values described damage in the regions with less defects well. The experimental strain fields fell at or between the modelled material cases, showcasing how much variation there can be in a typical filament wound material. Considering the 1.5 to 2 factor difference, a reduction of 40% in strength for the matrix can be considered reasonable.

Initial fiber failure could be characterized by an S-N curve measured locally (about 0.5 mm range) by DIC. Despite the curve´s high strength values, fiber failure was predicted conservatively within a decade of the experimental failure, much better than using traditional S-N curves obtained from typical coupon specimens. The model did, however, fall short of being able to correctly describe catastrophic fiber failure (accumulation of local fiber failures), due to its relatively simple nature and the sudden nature of catastrophic fiber failure. The experimental results showed that regions developing fluctuations in the strain fields were the areas where catastrophic fiber failure was initiated. The weak matrix model showed the same fluctuations in the FEA. These fluctuations can be measured by DIC and can be used as a warning for eminent failure. The results indicate that fiber failure and matrix failure are linked.

It can be concluded that the developed model is sufficient to model the complex strain and damage state in a split disk test if run with weak and strong matrix properties. The model is able to show how the strain fields develop and what shape the fields will attain in regions suspect to catastrophic fiber failure.

Author Contributions: Conceptualization, E.H., N.P.V. and A.T.E.; methodology, E.H. and A.T.E.; software, E.H.; validation, E.H., N.P.V. and A.T.E.; formal analysis, E.H.; investigation, E.H.; resources, E.H.; data curation, E.H.; writing—original draft preparation, E.H.; writing—review and editing, E.H., N.P.V. and A.T.E.; visualization, E.H.; supervision, N.P.V. and A.T.E.; project administration, E.H. and A.T.E.; funding acquisition, A.T.E. All authors have read and agreed to the published version of the manuscript.

Funding: This research was funded by Research Council of Norway, grant number 257653.

Acknowledgments: This work was performed within MoZEES, a Norwegian Centre for Environment-friendly Energy Research (FME), co-sponsored by the Research Council of Norway (project number 257653) and 40 partners from research, industry, and public sector.

Conflicts of Interest: The authors declare no conflict of interest.

Glossary

	General	Material Direction Specific
Material direction, with examples:		$_{ij}$
Fiber direction	-	$_{11}$
Matrix direction	-	$_{22}$
In plane shear direction	-	$_{12}$
Through thickness direction	-	$_{33}$
General sign of peak/max value	$\hat{}$	$\hat{}_{ij}$
Tensional property	$_{T}$	$_{ijT}$
Compressive property	$_{C}$	$_{ijC}$
Strain	ε	ε_{ij}
Residual strain	ε_{res}	$\varepsilon_{res,ij}$
Cycles	N	-
E-modulus	E	E_{ij}
Shear modulus	G	G_{ij}
Traction components:		
Normal component (Mode I)	$_{n}$	
First shear component (Mode II)	$_{s}$	
Second shear component (Mode III)	$_{t}$	
Max traction	t	t_n, t_s, t_t
Contact stiffness	K	K_n, K_s, K_t
Fracture energy	G	G_n, G_s, G_t
Separation	δ	$\delta_n, \delta_s, \delta_t$
Max separation	δ_f	$\delta_{fn}, \delta_{fs}, \delta_{ft}$
Max elastic separation	δ_0	$\delta_{0n}, \delta_{0s}, \delta_{0t}$
Property at a given number of cycles N	^{N}	$^{N}_{ij}$
Exposure factor		f_{ij}
Slope of S-N curve	α	α_{ij}
Origin of S-N curve	^{O}	$^{O}_{ij}$
Cumulative damage (Miner sum)	M	M_{ij}
Property in a load block in a Miner sum.		$_{k}$
Example of symbols:		
Intercept in tensional fatigue curve for fiber		$\hat{\varepsilon}^{O}_{11T}$
Max static strain in tensional transverse (matrix) direction		$\hat{\varepsilon}_{22T}$

References

1. US Departement of Energy (DOE)/GO-102005-1741. Hydrogen, fuel cells and infrastructure technologies program. Multi-Year Research. In *Development and Demonstration Plan*; US Departement of Energy: Washington, DC, USA, 2005.
2. Crawford, M. Virtual Testing of Composite Pressure Vessels. The American Society of Mechanical Engineers. 2020. Available online: https://www.asme.org/topics-resources/content/virtual-testing-of-composite-pressure-vessels (accessed on 17 June 2020).
3. Leh, D.; Saffré, P.; Francescato, P.; Arrieux, R. Multi-sequence dome lay-up simulations for hydrogen hyper-barcomposite pressure vessels. *Compos. Part A* **2013**, *52*, 106–117. [CrossRef]
4. Ribeiro, M.L.; Vandepitte, D.; Tita, V. Damage Model and Progressive Failure Analyses for Filament Wound Composite Laminates. *Appl. Compos. Mater.* **2013**, *20*, 975–992. [CrossRef]
5. Gentilleau, B.; Bertin, M.; Touchard, F.; Grandidier, J.-C. Stress analysis in specimens made of multi-layer polymer/composite used for hydrogen storage application: Comparison with experimental results. *Compos. Struct.* **2011**, *93*, 2760–2767. [CrossRef]
6. Berro Ramirez, J.P.; Halm, D.; Grandidier, J.-C.; Villalonga, S.; Nony, F. 700 bar type IV high pressure hydrogen storage vessel burst—Simulation and experimental validation. *Int. J. Hydrogen Energy* **2015**, *40*, 13183–13192. [CrossRef]
7. Turon, A.T. *Simulation of Delamination in Composites under Quasi-Static and Fatigue Loading Using Cohesive Zone Models*; University of Girona: Girona, Spain, 2006.
8. Talreja, R.; Watt, W. Fatigue of composite materials: Damage mechanisms and fatigue-life diagrams. *Proc. R. Soc.* **1981**, *378*, 1775.
9. Pupurs, A.; Varna, J. Modeling mechanical fatigue of UD composite: Multiple fiber breaks and debond growth. In Proceedings of the 5th International EEIGM/AMASE/FORGEMAT Conference on Advanced Materials Research, Nancy, France, 5 November 2009.
10. Curtis, P.T. Tensile fatigue mechanisms in unidirectional polymer matrix composite materials. *Int. J. Fatigue* **1991**, *13*, 377–382. [CrossRef]

11. Harik, V.M.; Klinger, J.R.; Bogetti, T.A. Low-cycle fatigue of unidirectional. *Composites Int. J. Fatigue* **2002**, *24*, 455–462. [CrossRef]
12. Lemaitre, J.; Sermage, J.P.; Desmorat, R. A two scale damage concept applied to fatigue. *Int. J. Fract.* **1999**, *97*, 67–81. [CrossRef]
13. Turon, A.; Costa, J.; Camanho, P.P.; Dávila, C.G. Simulation of Delamination in Composites under High-Cycle Fatigue. *Compos. Part A Appl. Sci. Manuf.* **2007**, *38*, 2270–2282. [CrossRef]
14. Mandell, J.F.; Huang, D.D.; McGarry, F.J. Fatigue of Glass and Carbon Fiber Reinforced Engineering Thermoplastics. *Polym. Compos.* **1981**, *2*, 137–144. [CrossRef]
15. Nixon-Pearson, O.J.; Hallett, S.R.; Harper, P.W.; Kawashita, L.F. Damage development in open-hole composite specimens in fatigue. Part 2: Numerical modelling. *Compos. Struct.* **2013**, *106*, 890–898. [CrossRef]
16. Harper, P.W.; Hallett, S.R. A fatigue degradation law for cohesive interface elements—Development and application to composite materials. *Int. J. Fatigue* **2010**, *32*, 1774–1787. [CrossRef]
17. NASA CompDam—Deformation Gradient Decomposition (DGD). NASA. 2019. Available online: https://github.com/nasa/CompDam_DGD (accessed on 20 January 2019).
18. Flatscher, T.; Pettermann, H.E. A constitutive model for fiber-reinforced polymer plies accounting for plasticity and brittle damage including softening—Implementation for implicit FEM. *Compos. Struct.* **2011**, *93*, 2241–2249. [CrossRef]
19. Gagani, A.I.; Kraukalis, A.; Sæter, E.; Vedvik, N.P.; Echtermeyer, A.T. A novel method for testing and determining ILSS for marine and offshore composites. *Compos. Struct.* **2019**, *220*, 431–440. [CrossRef]
20. Rozylo, P. Experimental-numerical study into the stability and failure of compressed thin-walled composite profiles using progressive failure analysis and cohesive zone model. *Compos. Struct.* **2021**, *257*, 113303. [CrossRef]
21. Brunbauer, J.; Gaier, C.; Pinter, G. Computational fatigue life prediction of continuously fibre reinforced multiaxial composites. *Compos. Part B* **2015**, *80*, 269–277. [CrossRef]
22. Safe Technology Limited. *Safe. Technology Limited: Produktinformationsblatt Fe-Safe/Composites Powered by He-Lius: Fatigue—Composite Durability Analysis Software for Finite Element Models*; Sheffield, Safe Technology Limited: Sheffield, UK, 2010.
23. Koch, I.; Zscheyge, M.; Tittmann, K.; Gude, M. Numerical fatigue analysis of CFRP components. *Compos. Struct.* **2017**, *168*, 392–401. [CrossRef]
24. Sevenois, R.D.B.; Garoz, D.; Gilabert, F.A.; Spronk, S.W.F.; Paepegem, W.V. Microscale based prediction of matrix crack initiation in UD composite plies subjected to multiaxial fatigue for all stress ratios and load levels. *Compos. Sci. Technol.* **2017**, *142*, 124–138. [CrossRef]
25. Chambers, A.R.; Earl, J.S.; Squires, C.A.; Suhot, M.A. The effect of voids on the flexural fatigue performance of unidirectional carbon fibre composites developed for wind turbine applications. *Int. J. Fatigue* **2006**, *28*, 1389–1398. [CrossRef]
26. Chowdhury, K.A.; Talreja, R.; Benzerga, A.A. Effects of Manufacturing-Induced Voids on Local Failure in Polymer-Based Composites. *J. Eng. Mater. Technol.* **2008**, *130*, 021010. [CrossRef]
27. Sisodia, S.; Gamstedt, E.K.; Edgren, F.; Varna, J. Effects of voids on quasi-static and tension fatigue behaviour of carbon-fibre composite laminates. *J. Compos. Mater.* **2014**, *49*, 2137–2148. [CrossRef]
28. Niewiadomski, P.; Hoła, J. Failure process of compressed self-compacting concrete modified with nanoparticles assessed by acoustic emission method. *Autom. Constr.* **2020**, *112*, 103111. [CrossRef]
29. Hugaas, E.; Echtermeyer, A. Filament wound composite fatigue mechanisms investigated with full field DIC strain monitoring. *Open Eng.* **2021**, *11*, 401–413. [CrossRef]
30. Hugaas, E.; Echtermeyer, A.T. Estimating S-N curves for local fiber dominated fatigue failure in ring specimens representing filament wound pressure vessels with damage. *Compos. Part C Open Access* **2021**, *5*, 100135. [CrossRef]
31. Golewski, G.L. Evaluation of fracture processes under shear with the use of DIC technique in fly ash concrete and accurate measurement of crack path lengths with the use of a new crack tip tracking method. *Measurement* **2021**, *181*, 109632. [CrossRef]
32. 3B. *HiPertex W2020 Datasheet*; 3B: Hoeilaart, Belgium, 5 May 2015.
33. Momentive. *Technical Datasheet Epikote Resin MGS RIMR 135 and Epikure Curing Agent MGS RIMH 134—RIMH 137*; Momentive: New York, NY, USA, 5 May 2006.
34. Hashin, Z. Cumulative damage theory for composite materials: Residual life and residual strength methods. *Compos. Sci. Technol.* **1985**, *23*, 1–19. [CrossRef]
35. Diehl, T. Modeling Surface-Bonded Structures with ABAQUS Cohesive Elements: Beam-Type Solutions. In Proceedings of the ABAQUS User's Conference, Boston, MA, USA, 25–27 May 2004.
36. Perillo, G. Numerical and Experimental Investigation of Impact Behaviour of GFRP Composiites. Ph.D. Thesis, NTNU—Norwegian University of Science and Technology, Trondheim, Norway, 2014.
37. Toubal, L.; Karama, M.; Lorrain, B. Damage evolution and infrared thermography in woven composite laminates under fatigue loading. *Int. J. Fatigue* **2006**, *28*, 1867–1872. [CrossRef]
38. Perillo, G.; Vedvik, N.P.; Echtermeyer, A.T. Numerical and experimental investigation of impact on filament wound glass reinforced epoxy pipe. *J. Compos. Mater.* **2014**, *49*, 723–738. [CrossRef]
39. Ramesh, T. Fatigue of Composite Materials. In *Modern Trends in Composite Laminates Mechanics*; Altenbach, H., Becker, W., Eds.; International Centre for Mechanical Sciences (Courses and Lectures); Springer: Vienna, Austria, 2003; Volume 448.
40. Zhang, Z.; Hartwig, G. Relation of damping and fatigue damage of unidirectional fibre composites. *Int. J. Fatigue* **2002**, *24*, 713–718. [CrossRef]

41. Broutman, L.J.; Sahu, S. A New Theory to Predict Cumulative Fatigue Damage in Fiberglass Reinforced Plastics. In Proceedings of the Composite Materials: Testing and Design (Second Conference), Anaheim, CA, USA, 20–22 April 1971; ASTM International: West Conshohocken, PA, USA, 1972; Volume ASTM STP 497, pp. 170–188.
42. Owen, M.J.; Bishop, P.T. Fatigue properties of glass-reinforced plastics containing a stress concentrator. *J. Phys. D Appl. Phys.* **1973**, *6*, 2057–2069. [CrossRef]
43. Eliopoulos, E.N.; Philippidis, T.P. A progressive damage simulation algorithm for GFRP composites under cyclic loading. Part I: Material constitutive model. *Compos. Sci. Technol.* **2011**, *71*, 742–749. [CrossRef]
44. Davies, P.; Kausch, H.H.; Williams, J.G. Round-robin interlaminar fracture testing of carbon-fibre-reinforced epoxy and PEEK composites. *Compos. Sci. Technol.* **1992**, *43*, 129–136. [CrossRef]
45. Tsai, G.-C. Design of Composite ENF Specimens and Conduct Three-Point Test to Calculate Mode II Fracture Toughness. In Proceedings of the 9th International Conference on Engineering Education, San Juan, Puerto Rico, 7 July 2006.
46. Davies, P.; Blackman, B.R.K.; Brunner, A.J. Standard Test Methods for Delamination Resistance of Composite Materials: Current Status. *Appl. Compos. Mater.* **1998**, *5*, 345–364. [CrossRef]
47. Chen, J.F.; Li, S.Q.; Bisby, L.A.; Ai, J. FRP rupture strains in the split-disk test. *Compos. Part B Eng.* **2011**, *42*, 962–972. [CrossRef]
48. Passipoularidis, V.A.; Philippidis, T.P. Fatigue life prediction in composites using progressive damage modelling under block and spectrum loading. *Int. J. Fatigue* **2011**, *33*, 132–144. [CrossRef]